B 2 The Structure of Complex Fluids [1]

G. Gompper
Institute of Complex Systems
Forschungszentrum Jülich GmbH

Contents

[1] Lecture Notes of the $43^{\rm rd}$ IFF Spring School "Scattering Methods for Condensed Matter Research: Towards Novel Applications at Future Sources" (Forschungszentrum Jülich, 2012). All rights reserved.

1 Introduction

Soft Matter Science investigates the structure and dynamics of macromolecules, macromolecular aggregates, and small particles in solution. The notion "Soft Matter" has been coined by Pierre-Gilles De Gennes, nobel prize winner 1991 for "his discovery that methods for the investigation of ordering phenomena in simple systems can be generalized to complex forms of matter, in particular for liquid crystals and polymers". The notion "Complex Fluids" is often used synonymously with Soft Matter.
The classical fields of Soft Matter Science are polymer solutions and melts, colloidal suspensions, and amphiphilic systems. The early days of the investigation of such systems dates back at least to the beginning of the last century. However, it has been recognized only in the 1980s and 1990s that these three classes of materials should really be seen as special cases of Soft Matter systems. The reasons for this realization is four-fold:

- All Soft Matter systems are characterized by a mesoscopic structural length scale, in the range of tens of nanometers to tens of micrometers.
- The systems are characterized by a typical energy scale comparable to the thermal energy k_BT (where k_B is Boltzmann's constant, and T is room temperature), so that thermal fluctuations play a large role.
- The constitutive macromolecules can have many architectures, which are intermediate between linear synthetic polymers, hard-sphere colloids, and short-chain amphiphilic molecules, as illustrated in Fig. 1.
- Many systems studied today contain components of different character, such as polymers and colloids, which is essential to construct new materials with tailored properties.

This chapter focuses on amphiphilic systems, because this is the archetypical example of structure formation in complex fluids. Here, the building blocks are amphiphilic molecules, which consist of a polar head and a non-polar hydrocarbon tail. Amphiphilic molecules are also often called "surfactants", as an abbreviation for **surf**ace **act**ive substance. Structure formation in mixtures with water and/or oil is then driven by the "hydrophobic effect" that polar and non-polar substances do not want to mix — a example from daily live is salad sauce, where the oil inevitably separates from the water after shaking or mixing. In oil-water-amphiphile mixtures, this leads to the formation of amphiphilic monolayers at the oil-water interface, and thereby to a reduction of the surface tension. In mixtures of water and amphiphilic molecules, bilayers form, in which the polar heads are directed towards the water and shield the hydrocarbon tails, which are buried inside the bilayer, from water contact. The resulting structures are shown schematically in Fig. 2. The formation of amphiphilic mono- or bilayers is only the first level of structure formation. On a second level, this aggregates are the building blocks of larger structures and mesophases. The understanding of the physical mechanisms of this structure formation, and how it can be revealed by scattering experiments, is the content of this chapter.
The behavior of other soft matter systems, in particular of polymer solutions and melts, will be explained in Chaps. B.6, E.2 and E.3.
The statistical physics of amphiphilic systems, membranes, and related subjects of structure formation in complex fluids, has been discussed in recent years in a many books and reviews, *inter alia* by Porte (1992) [3], Gompper & Schick (1994) [4], Gelbart et al. (1994) [5], Safran (1994) [6], Evans & Wennerström (1994) [7], Lipowsky and Sackmann [8], David et al. (1996)

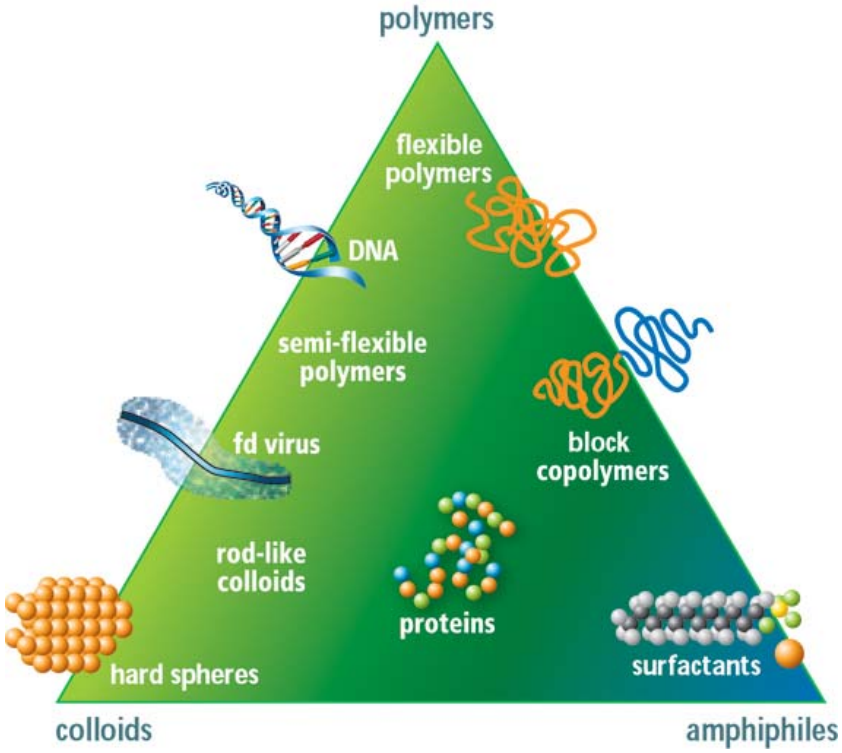

Fig. 1: *The "magic triangle" of soft matter, which shows that the classical fields of colloids, polymers and amphiphilic systems have merged into one. The aspect ratio (length/width) increases in the vertical direction, the amphiphilicity in the horizontal direction. From Refs. [1, 2].*

[9], Seifert (1997) [10], Gompper & Kroll (1997) [11], Cates & Evans (2000) [12], Dhont et al. (2002) [13], Nelson et al. (2004) [14], Witten & Pincus (2006) [15], Poon & Andelman (2006) [16], Dhont et al. (2008) [17], and Dhont et al. (2011) [18].

2 Oil-Water-Surfactant Mixtures

Phase Behavior of Water-Surfactant Mixtures — The experimental phase diagram of the binary mixture of the non-ionic surfactant $C_{12}E_5$ and water is shown in Fig. 3. The phase diagram is dominated by the two-phase coexistence between a dilute micellar phase L_1' and a more concentrated micellar phase L_1'' at low temperatures. Here, micelles are small spherical aggregates of amphiphilic molecules, with a hydrocarbon core and layer of polar heads outside, as shown schematically in Fig. 5 below. At high surfactant concentration, a lamellar phase L_α — a one-dimensional stack of surfactant bilayers separated by thin water films — is stable in this temperature range. At higher temperatures, the lamellar phase suddenly becomes stable already at very high dilution of only a few percent surfactant. Simultaneously, a sponge phase L_3 appears at even lower surfactant concentration.

Both the lamellar phase and the sponge phase are made of surfactant *bilayers*. Since the two leaflets of the bilayers are equivalent, these membranes cannot have a preferred curvature by symmetry (in contrast to monolayers, where in general a preferred curvature towards the oil- or

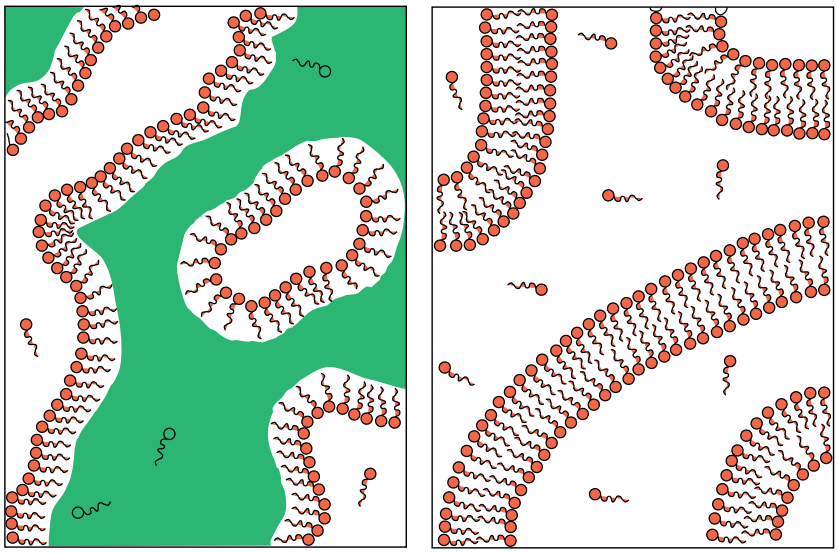

Fig. 2: *Amphiphilic molecules self-assemble into complex aggregates due to the hydrophobic effect. In mixtures with oil and water, they form monolayers at the water-oil interface. In mixtures with water, they form bilayers.*

water-side exists).

Lamellar Phase L_α **—** The stability of the lamellar phase at these strikingly low surfactant concentrations has caught the imagination of physicists in the late seventies of the last century. It was proposed by Helfrich (1978) [20] that this swelling behavior of the lamellar phase under the addition of water can be understood by the repulsive force generated by the suppression of long wave-length undulation modes of an individual membrane by its neighbors in the stack. This leads to a reduction of its entropy, and therefore to an increase of the free energy Δf per unit area, which was predicted to have the form [20]

$$\Delta f = c_\infty \frac{(k_B T)^2}{\kappa} d^{-2} \tag{1}$$

where d is the repeat distance of the lamellar phase, and κ is the bending rigidity of the bilayer. This behavior has since been investigated and verified experimentally (Safinya et al. 1986, 1989) [21, 22]. Monte Carlo simulations [23] give a value $c_\infty = 0.106$ for the value of the universal coefficient in Eq. (1).

Sponge Phase L_3 **—** Freeze-fracture microscopy reveals the mesoscopic structure of the sponge phase, as shown in Fig. 4. The fluid is frozen very rapidly to preserve its mesoscopic structure during the freezing process, then fractured into pieces. Fortunately, the fracture surface follows preferentially the midplane of the bilayer. Therefore, the three-dimensional structure of the membrane is revealed by this technique. Fig. 4 demonstrates impressively that the sponge phase is a complicated network of water channels, which are separated by membranes with a locally *saddle-shaped* structure.

The "sponge phase" has gotten it's name because its structure resembles the structure of a *sea-water* sponge (compare Fig. 4). The pore space of the sea-water sponge has to be connected in order for the water to be able to penetrate the sponge; its solid component has also to be connected to keep the sponge together. Thus, both objects are "bicontinuous" (see below).

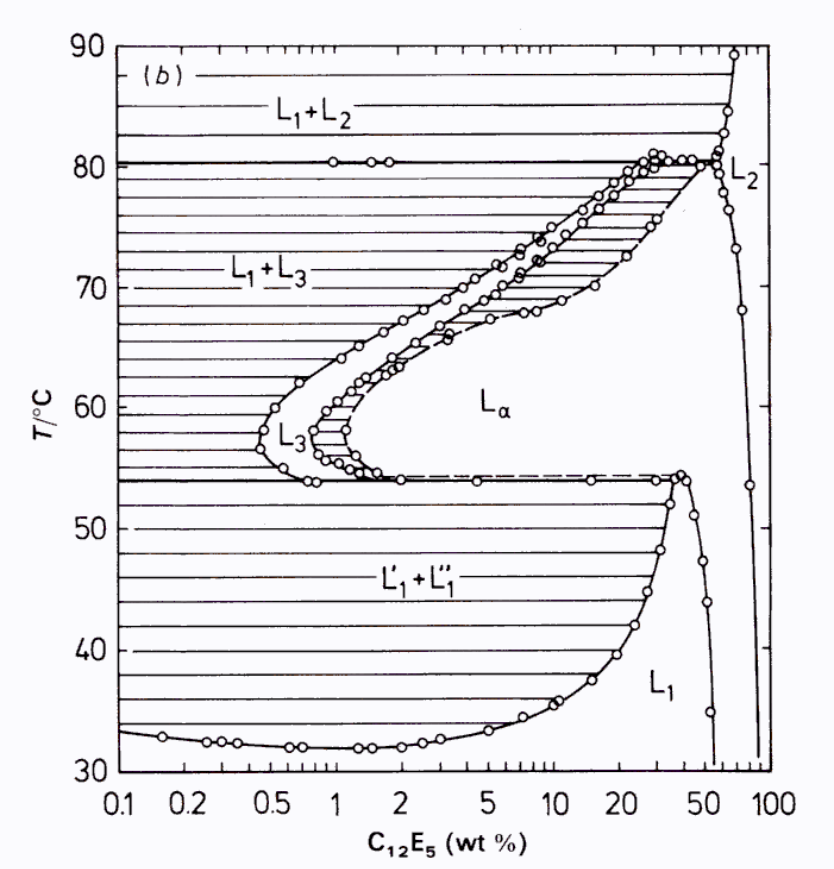

Fig. 3: *Experimental phase diagram of the binary mixture of $C_{12}E_5$ and water (Strey et al. 1990) [19]. The phase diagram is dominated by the two-phase coexistence between a dilute (L_1') and a more concentrated (L_1'') micellar phase at low temperatures. At higher temperatures, the lamellar phase (L_α) becomes stable already at high dilution of only a few percent surfactant. Simultaneously, a sponge (L_3) phase appears at even lower surfactant concentration. The phase at high surfactant concentration (L_2) is an inverted micellar phase (with surfactant tails pointing outwards). The hatched areas are two-phase coexistence regions. Note the logarithmic scale of the abscissa.*

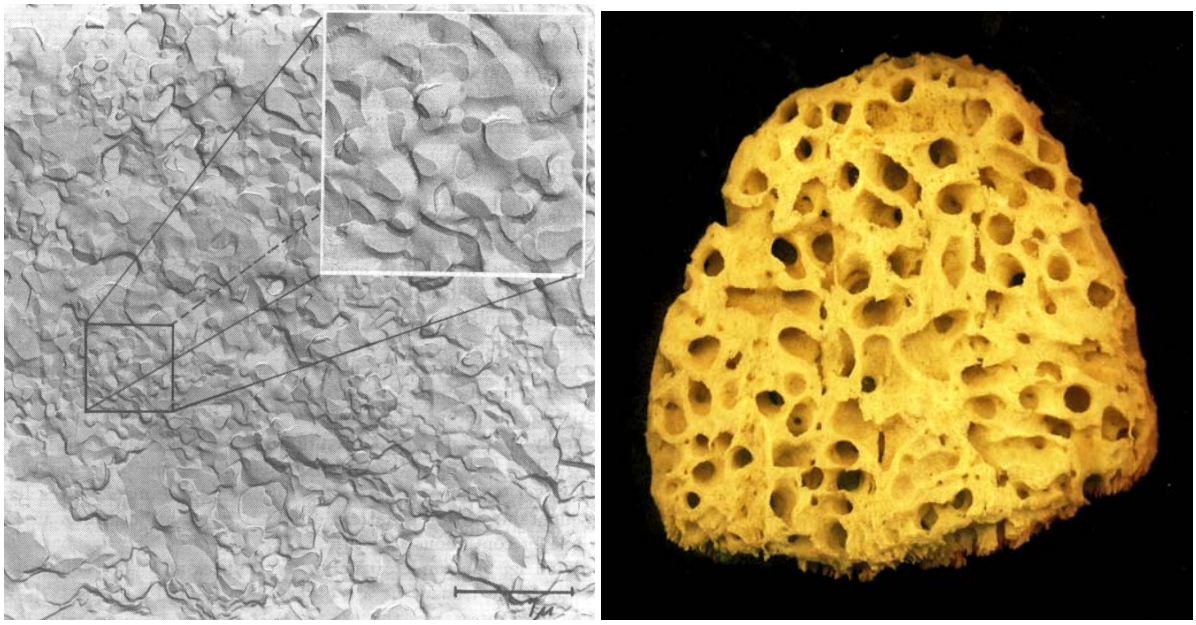

Fig. 4: *Left: Freeze-fracture-microscopy picture of a sponge phase in the system water/NaCl and AOT (Strey et al. 1992) [24]. Note the local saddle-shape structure of the membrane, which can be seen most clearly in the inset. Right: A sea-water sponge.*

However, the length scales are very different.

Microemulsions — When oil is added as a third component to a mixture of water and surfactant, the phase diagram obviously gets considerable more complicated [4], as shown schematically in Fig. 5. The spontaneous curvature of the monolayer membrane is in general non-zero in these systems. For most non-ionic surfactants, the spontaneous curvature depends sensitively and approximately linearly on temperature (compare Sec. 5), with curvature towards the oil-side at lower temperatures and curvature towards the water-side at higher temperatures (this can be understood by the diminishing hydration shell of the polar heads with increasing temperature). Therefore, the spontaneous curvature vanishes for one particular temperature, the hydrophobic-hydrophilic-balance temperature $\bar{T}$. In a temperature interval around $\bar{T}$, a phase is stable, which is macroscopically homogeneous and isotropic, and which contains equal amounts of oil and water. This phase is called a *microemulsion* . It has a very similar mesoscopic structure as the sponge phase:

- The membrane in the sponge is a bilayer, in the microemulsion it is a monolayer.
- The microemulsion consists of network of oil- and water-channels, which are separated by a surfactant monolayer. The sponge phase consists of (at least) two distinct networks of water-channels, which are separated by a bilayer.

A microemulsion is called *bicontinuous*, because both the oil- and the water-networks span the whole system. Since the sponge phase has an equivalent mesoscopic structure with two networks of water channels, it is also called bicontinuous.

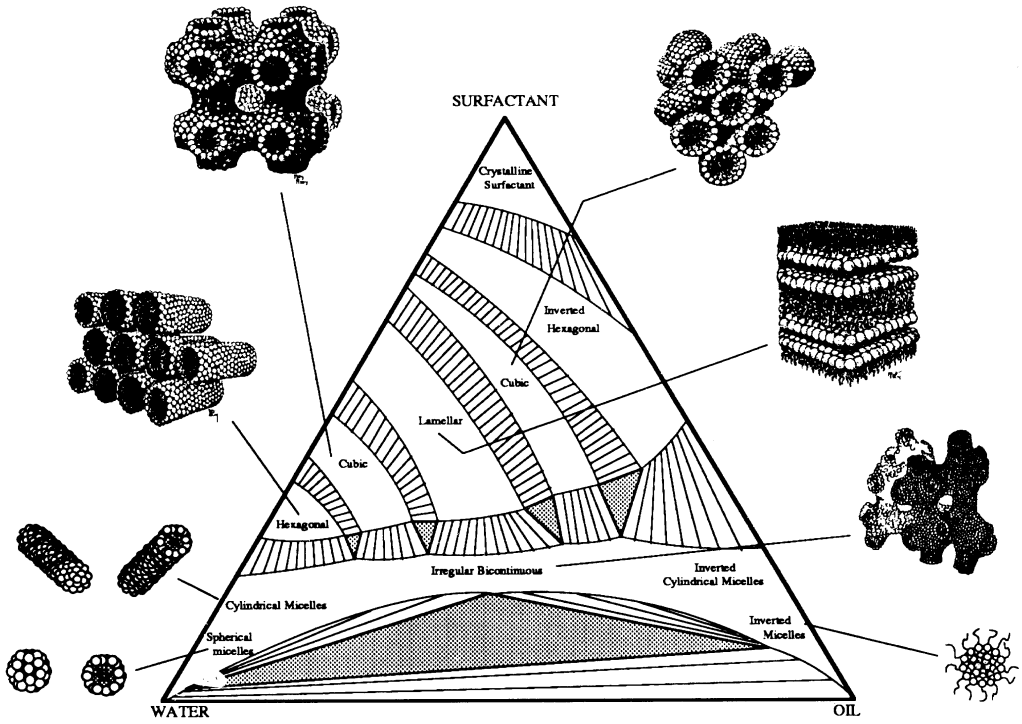

Fig. 5: *Schematic phase diagram of ternary amphiphilic systems at fixed temperature. From Davis et al. (1987) [25].*

3 Theoretical Approaches

3.1 Length Scales

A theoretical model always depends on the type of phenomena to be studied, and on the basic length scales to be described. This is not much different from experimental studies, where different techniques are appropriate for different ranges of length scales. For oil-water-surfactant mixtures, the different levels of descriptions, the appropriate length scales, and the the corresponding degrees of freedom, are illustrated in Fig. 6. On the molecular level, we are dealing with a three-component mixture of different molecules. The length scale is therefore atomistic, and the degrees of freedom are the atomic coordinates. This is a lot of information, which is only partially useful for a structured fluid with large oil-rich and water-rich domains. Therefore, we can zoom out a bit and only consider the concentrations fields, which are averaged over the local molecular conformations and orientations. On this level, we can already see that surfactant assembles at the mesoscopic oil-water interface. However, the domain structure is still difficult to describe. Thus, if we are interested in the shape and topology of the interfaces, we have to step back even further, and describe the membrane as a mathematical surface, with its shape and fluctuations controlled by curvature elasticity.

For the calculation of phase behavior and scattering intensities, the descriptions of the concentration level and on the membrane level are particularly useful.

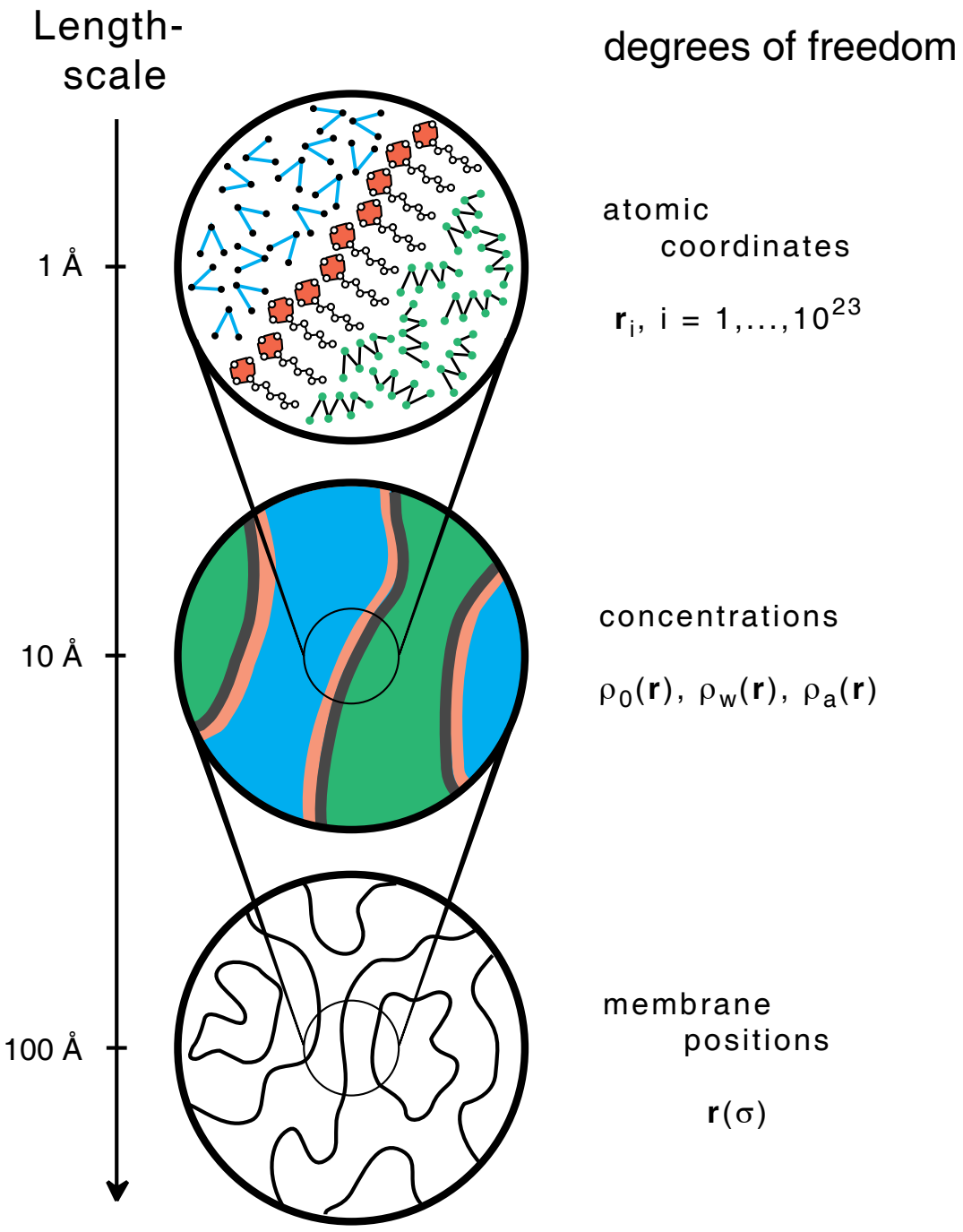

Fig. 6: *Modeling microemulsion structure on different length scales. The basic degrees of freedom on each level of coarse graining are indicated.*

3.2 Membrane Model

Curvature Energy and Fluctuating Surfaces — We want to try to understand the structure and phase behavior of binary mixtures of water and surfactant on the basis of a model, in which the surfactant film is described by a surface, whose shapes and fluctuations are controlled by the curvature energy (2). First attempts for such a description go back to Helfrich (1973) [26], Scriven (1976) [27], de Gennes and Taupin (1982) [28], and Safran et al. (1986) [29].
The energy functional of a *fluid membrane* must satisfy the following conditions

- Motion invariance:
  The energy must be invariant under translations and rotations of the whole membrane
- Reparametrization invariance:
  Since the molecules can diffuse freely within the membrane, no preferred coordinate system can exist — which would correspond physically to a labeling of distinct constitutive elements of the membrane. Therefore, the energy must be invariant under a change of the coordinate system.

These conditions imply that in an expansion in powers of the inverse radii of curvature, the curvature energy to leading order is given by [30, 26]

$$\mathcal{H}_{curv} = \int dS \left[\gamma + 2\kappa(H - c_0)^2 + \bar{\kappa}K + ...\right] \tag{2}$$

where the integration is over the whole membrane surface,

$$2H = c_1 + c_2 \quad , \quad K = c_1 c_2 \tag{3}$$

are the mean and Gaussian curvatures, respectively, which are expressed in terms of the principal curvatures $c_1 = 1/R_1$ and $c_2 = 1/R_2$ at each point of the membrane, compare Fig. 7. It is interesting to note that H and K are the trace and determinant of the curvature tensor, and therefore satisfy the invariance principles stated above. The parameters γ, κ, $\bar{\kappa}$ and c_0 are the elastic constants of the membrane, which depend on the structure and interactions of the constitutive molecules. Their physical meaning is:

- γ is the surface tension,
- κ is the bending rigidity,
- c_0 is the spontaneous (or preferred) curvature,
- $\bar{\kappa}$ is the saddle-splay modulus – relevant only for topology changes.

From a statistical mechanics point of view, the calculation of the thermodynamic properties of an ensemble of fluctuating surfaces is a formidable problem. It amounts to calculating the partition function

$$Z = \sum_{topologies} \int' \mathcal{D}\mathbf{R}(\underline{\sigma}) \exp\{\mathcal{H}[\mathbf{R}(\underline{\sigma})]/k_B T\} \tag{4}$$

where $\int' \mathcal{D}\mathbf{R}(\underline{\sigma})$ denotes an integration over all possible shapes with parametrization $\mathbf{R}(\underline{\sigma})$ of the surface at fixed topology, where $\underline{\sigma}$ is a two-dimensional coordinate system on the surface. However, this integral cannot be just over all possible parametrizations $\mathbf{R}(\underline{\sigma})$ of a surface of

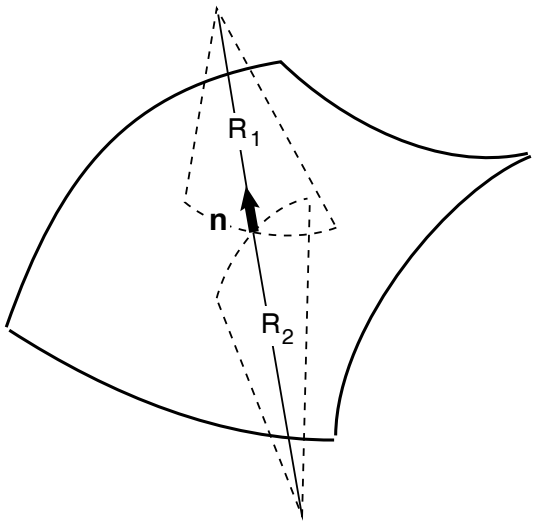

Fig. 7: *The two principal radii of curvature, R_1 and R_2, of a point on the surface.*

fixed topology, but has to be restricted to those parametrizations, which lead to physically different shapes in the embedding space; this is indicated by the prime. Finally, the contributions off all different topologies have to be summed over. It is clear that this problem is sufficiently complex that no exact solution will be found anytime soon. Therefore, approximations have to be made in order to get some insight into the behavior of these phases.

Energy Considerations — Let us first take a closer look at the curvature *energy* itself, and consider the effect of fluctuations in a second step. It is easily seen that for $c_0 = 0$ the curvature Hamiltonian (2) can be rewritten in the form

$$E = \int dS \left[\frac{1}{2}\kappa_+ \left(\frac{1}{R_1} + \frac{1}{R_2} \right)^2 + \frac{1}{2}\kappa_- \left(\frac{1}{R_1} - \frac{1}{R_2} \right)^2 \right] \tag{5}$$

with

$$\kappa_+ = \kappa + \frac{1}{2}\bar{\kappa} \quad , \quad \kappa_- = -\frac{1}{2}\bar{\kappa} \tag{6}$$

This form is convenient to show that the stability of lamellar phase requires

$$\kappa_+ > 0 \ , \ \kappa_- > 0 \tag{7}$$

since otherwise the energy of the system could be lowered without bounds by making the term with negative amplitude very large in magnitude. With Eq. (6), the stability conditions (7) are equivalent to

$$-2\kappa < \bar{\kappa} < 0 \tag{8}$$

Instabilities occur as κ_+ or κ_- approach zero:

- For $\kappa_+ \to 0$, it costs very little energy to make $|c_1 + c_2|$ large, as long as $|c_1 - c_2|$ remains small. Thus, in this limit it costs a very small energy to form small spherical objects with $c_1 \simeq c_2$, which in the case of monolayers are called micelles, in the case of of bilayers *vesicles*.

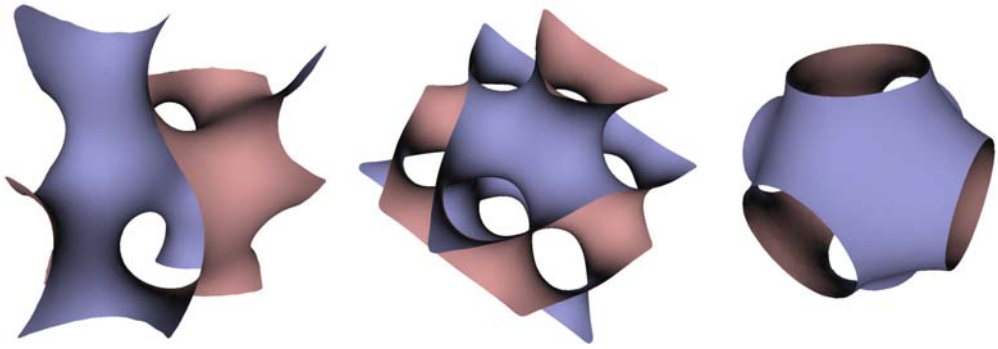

Fig. 8: *The three most important triply periodic minimal surfaces (TPMS) of cubic symmetry: Schwarz P-surface (right), Schwarz D-surface (middle), and Schoen's gyroid surface (left) [31].*

- For $\kappa_- \to 0$, it costs very little energy to make $|c_1 - c_2|$ large, as long as $|c_1 + c_2|$ remains small. Thus, in this limit it costs a very small energy to form surfaces with $c_1 \simeq -c_2$ and small domain size, such as microemulsions or sponge phases.

It is interesting to note that sufaces with $c_1 = -c_2$ have been studied extensively for more than 100 years. These surfaces are called *minimal surfaces*. In the context of amphiphilic systems, triply periodic minimal surfaces (TPMS) of cubic symmetry, shown in Fig. 8, are particularly relevant. These phases are also often called *plumber's nightmare phases*, because this multiply connected system of tubes would be almost impossible for a plumber to prevent such a structure from leaking.

Scaling Considerations — Let us consider an arbitrarily shaped piece of membrane with fixed geometry. Let the local curvatures be denoted by c_i, and the curvature energy of this patch be E_b. When this membrane piece is rescaled uniformly by a scale factor λ — i.e. the "shape" remains the same but the size changes — then the new local curvatures become $c_i' = \lambda^{-1} c_i$, and the curvature energy changes to

$$\begin{aligned} E_b' &= \int dS' \left\{ 2\kappa H'^2 + \bar{\kappa} K' \right\} \\ &= \int dS \lambda^2 \left\{ 2\kappa \lambda^{-2} H^2 + \bar{\kappa} \lambda^{-2} K \right\} \equiv E_b \end{aligned} \tag{9}$$

Thus, the curvature energy remains invariant under uniform scale transformations. This results implies immediately that the energy *density*, which is the energy *per unit volume*, depends on the surface-to-volume ratio, S/V, which is proportional to the amphiphile concentration, as [32]

$$E_b/V \sim (S/V)^3 \tag{10}$$

Eq. (10) shows that the curvature energies of all membrane structures scale in exactly the same way (although with different prefactors), so that an intersection of the energy curves for different structures as a function of S/V cannot occur. This result allows an important conclusion. On the basis of the curvature energy alone, without thermal fluctuations, we will not be able to understand transitions between different mesophases as the amphiphile concentration is varied, such as the lamellar-to-sponge transition in Fig. 3 at fixed temperature. It must be the *entropy*

which is responsible for these transitions.

Membrane Fluctuations — The thermal fluctuations on small scales — i.e. small compared to the typical domain size of a sponge phase, or small compared to the average separation of membranes in a lamellar phase — modify the curvature elasticity on larger scales. This effect can be easily demonstrated with a sheet of paper for *polymerized* membranes (with fixed connectivity of neighboring molecules): A corrugated sheet has a higher bending rigidity on scales larger than the characteristic ripples than a smooth sheet. Thus, "fluctuations" increase the rigidity in this case. In *fluid* membranes, fluctuations have the opposite effect of softening the rigidity on larger scales. There is no macroscopic example to demonstrate this effect. It follows from renormalization group calculations [33, 34], which show that thermal fluctuations lead to renormalized, *scale-dependent* rigidities κ^R, $\bar{\kappa}^R$ of the form

$$\kappa_R(\xi) = \kappa - \alpha \frac{k_B T}{4\pi} \ln(\xi/a) \tag{11}$$

$$\bar{\kappa}_R(\xi) = \bar{\kappa} - \bar{\alpha} \frac{k_B T}{4\pi} \ln(\xi/a) \tag{12}$$

with $\alpha = 3$ and $\bar{\alpha} = -10/3$ (Peliti & Leibler 1985, David 1989) [33, 35]. This implies immediately that the elastic moduli of Eq. (5) are also renormalized, and are given by

$$\kappa_\pm^R(\xi) = \kappa_\pm - \alpha_\pm \frac{k_B T}{4\pi} \ln(\xi/a) \tag{13}$$

with

$$\alpha_+ = \alpha + \frac{1}{2}\bar{\alpha} = \frac{4}{3} \quad , \quad \alpha_- = -\frac{1}{2}\bar{\alpha} = \frac{5}{3} \tag{14}$$

Phase Behavior — When the fluctuation on short scales are taken into account, the instabilities of the lamellar phase discussed above now occur where the *renormalized* rigidities vanish, i.e. at $\kappa_\pm^R(\xi) = 0$. The length scale ξ, where the renormalization is cut off, is determined by the average separation of neighboring membranes, which is given by the membrane volume fraction

$$\Psi \equiv \frac{aS}{V} = a/\xi \tag{15}$$

where a is again a molecular scale, here the length of the amphiphiles. This finally implies (Morse 1994) [36]

$$\ln(\Psi) = -\frac{4\pi}{\alpha_\pm} \frac{\kappa_\pm}{k_B T} \tag{16}$$

The phase diagram, which is predicted on the basis of this calculation, is shown in Fig. 9. This phase diagram does not only contain the instability lines (16), but also results of a somewhat more detailed calculation, in which estimates of the free energies of the sponge phase (based on an approximation by minimal surfaces, so that the free energy is taken to be $\bar{\kappa}_R(\xi) \int dS\ K$) and of the lamellar phase (based on the steric repulsion expression (1)) are compared. Fig. 9 shows that the two results are in good agreement.

The phase diagram is dominated by a V-shaped region, where the lamellar phase is stable. With decreasing amphiphile concentration, a phase transition to the sponge phase occurs for $0 > \bar{\kappa}/\kappa > -10/9$, while a transition to a vesicle phase occurs for $-10/9 > \bar{\kappa}/\kappa > -2$. The sponge phase exists only in a narrow strip parallel to the instability line. When the amphiphile concentration is decreased further, *emulsification failure* occurs, i.e. the sponge phase cannot take up any more water, and therefore coexists with an (almost pure) water phase at these low membrane volume fractions.

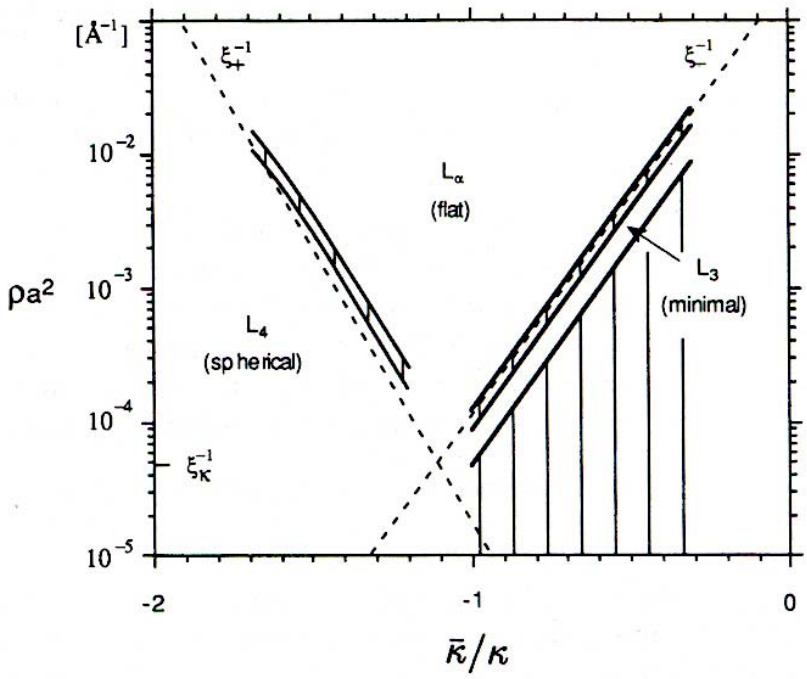

Fig. 9: *Phase diagram of binary or balanced ternary amphiphile mixtures, as predicted on the basis of the renormalization of the bending rigidity κ and the saddle-splay modulus $\bar{\kappa}$, for fixed $\kappa/k_BT = 2$ (Morse 1994) [36]. The phase behavior is shown as a function of the membrane volume fraction Ψ (denoted here ρa^2) and the saddle-splay modulus $\bar{\kappa}$. L_3 denotes the sponge phase, L_4 a vesicle phase. The two dashed lines are the stability boundaries (16), with the left line corresponding to $\kappa_+^R = 0$, the right line to $\kappa_-^R = 0$.*

3.3 Ginzburg-Landau Model

An alternative description of microemulsion starts from the point of view of ternary mixtures with three spatially varying concentration fields $\rho_o(\mathbf{r})$, $\rho_w(\mathbf{r})$, and $\rho_s(\mathbf{r})$ for oil, water, and surfactant, respectively. Such a description has been used extensively for near-critical binary mixtures. For incompressible of, say, oil and water, $\rho_o(\mathbf{r}) + \rho_w(\mathbf{r})$ =const., so that only the local concentration difference $\phi(\mathbf{r}) \equiv \rho_o(\mathbf{r}) - \rho_w(\mathbf{r})$, which is denoted "order parameter field", has to be considered. The model is then defined by the free energy functional

$$\mathcal{F}[\phi] = \frac{1}{2}\int d^3r \left[b_0(\nabla\phi(\mathbf{r}))^2 + f(\phi)\right] \tag{17}$$

Here, the free energy density of homogeneous order parameter fields has two minima below the critical temperature T_c, corresponding to the order parameters of the coexisting oil-rich and water-rich phases, and is usually written in an expansion for small order parameters as $f(\phi) = \tau\phi^2 + g\phi^4$, where $\tau = (T - T_c)/T_c < 0$ measures the distance from the critical point. Above T_c, where $\tau > 0$, $f(\phi)$ has a single minimum at $\phi = 0$ (completely mixed state). The first term on the right-hand side of Eq. (17), with $b_0 > 0$, penalizes inhomogeneous order-parameter configurations, and is therefore closely related to the oil-water interface tension.

This approach can be generalized to ternary amphiphilic systems [37]. In the simplest case, where the surfactant molecules are assumed to mostly populate the microscopic oil-water interface, the surfactant density does not have to be taken into account as an additional order parameter. Instead, it modifies only the structure of the free-energy functional, which now becomes [37]

$$\mathcal{F}[\phi] = \frac{1}{2}\int d^3r \left[c_0(\nabla^2\phi(\mathbf{r}))^2 + b(\phi)(\nabla\phi(\mathbf{r}))^2 + f(\phi)\right] \tag{18}$$

Here, the function $f(\phi)$ has now three minima, corresponding to the coexisting oil-rich, water-rich and microemulsion phases. The function $b(\phi)$ has a single minimum in the microemulsion phase, with $b_0 = b(0) < 0$; this negative value of the gradient-term in Eq. (18) corresponds to the fact that the system gains free energy by increasing the amount of oil-water interface area. This growth is limited by the first term in Eq. (18), with $c_0 > 0$, which is closely related to the bending rigidity of the surfactant layer.

In the microemulsion phase, where $\langle\phi(\mathbf{r})\rangle = 0$, the free-energy functional (18) can be expanded to quadratic order in the order-parameter fluctuations,

$$\mathcal{F}[\phi] = \frac{1}{2}\int d^3r \left[c_0(\nabla^2\phi(\mathbf{r}))^2 + b_0(\nabla\phi(\mathbf{r}))^2 + a_0\phi^2\right] \tag{19}$$

In this approximation, the scattering intensity can be calculated exactly, as explained in Appendix A, with the result [38]

$$I(q) = \frac{1}{c_0 q^4 + b_0 q^2 + a_0} \tag{20}$$

The negative value of b_0 implies that there is a scattering peak at non-zero wave vector. It was shown already more than 20 years ago by Teubner & Strey (1987) [38] that the functional form of Eq. (20) indeed fits experimental scattering data very well, compare Fig. 10.

The correlation function in real space is obtained from the scattering intensity by Fourier transformation, as explained in detail in Chap. A.5. Fortunately, the form of Eq. (20) is simple enough that this Fourier transformation can be done analytically, so that [38, 4]

$$G(r) = \int \frac{d^2q}{(2\pi)^2} I(q) e^{-i\mathbf{q}\cdot\mathbf{r}} \sim \frac{1}{r} e^{-r/\xi} \sin k_0 r \tag{21}$$

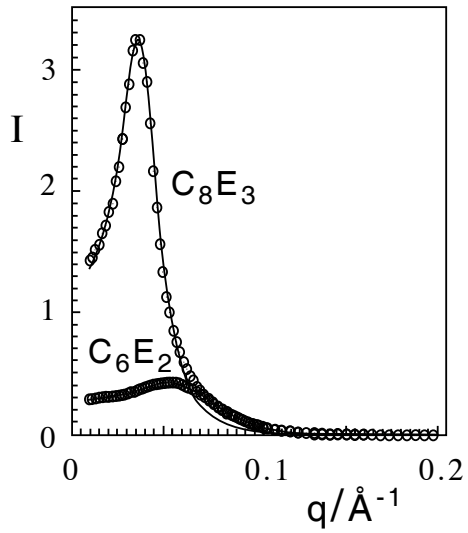

Fig. 10: *The scattering intensity $I(q)$ of a balanced microemulsion in bulk contrast for two different surfactants. The data are very well fitted by the functional form of Eq. (20) (Teubner & Strey 1987) [38].*

with *characteristic wave vector* k_0 and *correlation length* ξ, where

$$k_0 = \frac{1}{2}\left[2\sqrt{a_0/c_0} - b_0/c_0\right]^{1/2} \quad , \quad \xi^{-1} = \frac{1}{2}\left[2\sqrt{a_0/c_0} + b_0/c_0\right]^{1/2} \tag{22}$$

3.4 Gaussian Random Fields

A description of microemulsions and sponge phases, which is closely related to the Ginzburg-Landau approach, is to employ *level surfaces* of a scalar field $\Phi(\mathbf{r})$, with $\mathbf{r} \in \mathbb{R}^3$, which are defined by

$$\Phi(\mathbf{r}) = \alpha \tag{23}$$

This implicitly defines a surface in three-dimensional space. An illustration of this concept is shown in Fig. 11, where the level "surfaces" are shown for a scalar field in two dimensions. Thermal fluctuations of the scalar field $\Phi(\mathbf{r})$ — according to a Boltzmann weight $\exp(-\mathcal{H}_0)$ — then imply fluctuations of the level surfaces. The properties of the membranes are therefore induced by the statistical mechanics of the scalar field Φ, as they are in the Ginzburg-Landau model.
A particularly useful case are *Gaussian random fields* (GRF) , where the fluctuations of Φ are controlled by a Boltzmann weight with a *quadratic* Hamiltonian

$$\mathcal{H}_0 = \frac{1}{2}\int d^3r \Phi(\mathbf{r})\nu^{-1}(|\mathbf{r}-\mathbf{r}'|)\Phi(\mathbf{r}') \tag{24}$$

with *spectral density* $\nu(\mathbf{r}-\mathbf{r}')$. Requirements on $\nu^{-1}(|\mathbf{r}-\mathbf{r}'|)$ are that it decays sufficiently fast for large $|\mathbf{r}-\mathbf{r}'|$ so that the integral and the second and fourth moments are finite. The normalization

$$\langle\Phi(\mathbf{r})\rangle = 0 \quad , \quad \langle\Phi(\mathbf{r})^2\rangle = 1 \tag{25}$$

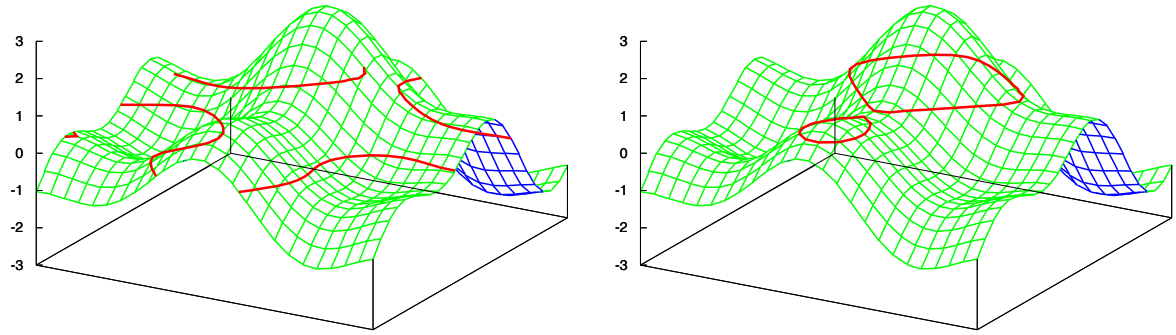

Fig. 11: *Level "surfaces" of a scalar field $\Phi(\mathbf{r})$, with $\langle\Phi(\mathbf{r})\rangle = 0$. For illustration purposes, $\mathbf{r} \in \mathbb{R}^2$, so that the level "surfaces" are in fact lines in this case. Left: Level surface (red lines) for $\alpha = 0$, so that the surface has no preferred curvature, $\langle H\rangle = 0$, and a sponge-like structure can be envisaged. Right: Level surface (red lines) for $\alpha = 1$, so that the level surface bends preferentially to one side, and droplet-like structures can be seen.*

is usually employed, where the first identity follows immediately from the $\Phi \to -\Phi$ symmetry of the Hamiltonian, while the second identity implies the normalization $\int d^3k\ \nu(k) = (2\pi)^3$. The advantage of the Gaussian random field model is that all averages can be calculated exactly. In particular, the *average geometry* of the level surfaces can be calculated for Gaussian random fields (GRF), with the analytical results (Teubner 1991) [39]:

$$S/V = \frac{2}{\pi}\exp[-\alpha^2/2]\sqrt{\frac{1}{3}\langle q^2\rangle_\nu} \tag{26}$$

$$\langle K\rangle = -\frac{1}{6}\langle q^2\rangle_\nu(1-\alpha^2)\,, \tag{27}$$

$$\langle H\rangle = \frac{1}{2}\alpha\sqrt{\frac{\pi}{6}\langle q^2\rangle_\nu}\,, \tag{28}$$

$$\langle H^2\rangle = \langle K\rangle + \frac{1}{5}\frac{\langle q^4\rangle_\nu}{\langle q^2\rangle_\nu} \tag{29}$$

where

$$\langle q^n\rangle_\nu \equiv \int \frac{d^3q}{(2\pi)^3} q^n \nu(q) \tag{30}$$

The calculation of the surface density S/V is sketched in Appendix B to illustrate the calculation of geometrical averages for Gaussian random fields.
The results (26) to (29) imply some interesting conclusions for the symmetric case $\alpha = 0$:

- Eq. (28) shows that mean curvature vanishes, $\langle H\rangle \equiv 0$, so that $\alpha = 0$ corresponds to a balanced system, such as in sponge phases or balanced microemulsions. Compare Fig. 11.

- From Eq. (27), we find $\langle K\rangle = -\frac{1}{6}\langle q^2\rangle_\nu < 0$; this implies that the average geometry of level surfaces in Gaussian random fields is *saddle-shaped*. Eqs. (27) and (26) can be combined to give the dimensionless quantity $\langle K\rangle(S/V)^{-2} = -\pi^2/8 = -1.234$, which

characterizes the topology of a characteristic "unit cell" of the sponge phase. It is important to note that this number is *universal* in the Gaussian random field model, since it is completely independent of the spectral density ν.

3.5 Variational Approach

In Sec. 3.4, the spectral density ν has never been specified. The application of the Gaussian random field model to sponge phases therefore remains qualitative on this level [40, 41, 39]. What is missing is a relation of the spectral density ν to the Hamiltonian which describes the system under consideration. For a membrane ensemble controlled by the curvature energy, considerable progress can be made by employing the Gaussian random field model in a variational approach (Pieruschka & Safran 1993) [42].

The variational approach is based on the Gibbs-Bogoliubov-Feynman inequality [43, 44]. It relates the energies and free energies of the system under consideration (in our case the membrane ensemble with curvature energy) to a reference system, which can be treated more easily (in our case the Gaussian random field model).

Let the full system be described by a Hamiltonian $\mathcal{H}$ and have free energy F, and the reference system be described by Hamiltonian $\mathcal{H}_0$ and have free energy F_0. The Gibbs-Bogoliubov-Feynman inequality is based on the inequality $\langle \exp(f) \rangle \geq \exp\langle f \rangle$ for any function $f \in \mathbb{R}$ [44]. This implies

$$F \leq F_0 + \langle \mathcal{H} - \mathcal{H}_0 \rangle_0 \tag{31}$$

The main idea of the variational approach is then to choose a reference system with free parameters, which can be used to find an optimal (i.e. lowest) upper bound for the free energy of the full system.

The application of this approach to membrane ensembles requires the calculation of $\langle \mathcal{H} \rangle_0$ and F_0. The average curvature energy is

$$\langle \mathcal{H}_{curv} \rangle_0 = S \left(2\kappa \langle H^2 \rangle_0 + \bar{\kappa} \langle K \rangle_0 \right) \tag{32}$$

which can be easily expressed as a functional of the spectral density with Eqs. (26)-(29). The calculation of the free energy of a Gaussian model is a standard problem of statistical field theory, as described for example in detail in Ref. [44], and has the result

$$F_0 = -\frac{1}{2} \int \frac{d^3k}{(2\pi)^3} \ln(\nu(k)) \tag{33}$$

Functional differentiation of Eq. (31) with Eqs. (32) and (33) then gives the *optimal spectral density* (Pieruschka & Safran 1995) [45]

$$\nu(q) = \frac{1}{cq^4 + bq^2 + a} \tag{34}$$

where a, b, and c are now functions of κ and S/V.

The spectral density (34) can be identified with the scattering intensity $I(q)$ in bulk contrast of ternary microemulsions, i.e. with scattering contrast between oil and water, in the same way as discussed for the Ginzburg-Landau model in Sec. 3.3 above.

With the use of Eq. (22), the results of the variational approach then imply for the characteristic length scales in the correlation function (for large κ/k_BT):

$$k_0 \sim S/V \quad , \quad \xi \sim \kappa (S/V)^{-1} \quad , \quad k_0 \xi \sim \kappa \tag{35}$$

Thus, the wave vector k_0 increases linearly with the amphiphile concentration, while the correlation length ξ decreases. However, the dimensionless ratio $k_0\xi$ of the two length scales, which characterize a microemulsion or sponge phase, is predicted to be *independent* of the amphiphile concentration, and only to depend on the bending rigidity. These are very specific predictions, which can be tested experimentally and by simulations.

3.6 Comparison of Theoretical Approaches

We have now predictions by two different theoretical models, which we abbreviate by the names 'Fluctuating Membranes" and "Gaussian Random Fields". It is instructive to summarize the main points discussed above:

- "Fluctuating Membranes" and "Gaussian Random Fields" are *complementary models*
- The variational approach provides a link between these models
- A direct comparison is possible for the *free energy*:
  Fluctuating Membranes —

$$\begin{aligned} f = F/V &\sim [\kappa_R(\Psi) + \bar{\kappa}_R(\Psi)]\Psi^3 \\ &= [A + B\ln(\Psi)]\Psi^3 \end{aligned} \tag{36}$$

  as shown in Refs. [46, 47, 32, 3].
  Gaussian Random Fields —

$$f = F/V = A'\Psi^3 + B'\ln(\Psi) \tag{37}$$

  as derived in Ref. [45]. It is obvious from the comparison of these two equations that although the results look similar they do *not* agree!

4 Monte Carlo Simulations of Dynamically Triangulated Surfaces

As in all entropically dominated, strongly fluctuating systems, simulation methods provide a very important tool to obtain information about the system properties, which are not easily accessible by purely analytical approaches. For sufficiently small systems, thermal averages can be calculated by simulation techniques with very high precision. The extrapolation to large system sizes is sometimes difficult, but often possible with good reliability.

Motivation — What are the particular reasons to apply simulations to membrane ensembles:

- Clarify the discrepancy between functional forms of the free energies of the "Fluctuating Membranes" and the "Gaussian Random Field" approaches, Eqs. (36) and (37).
- Different results have been obtained for the universal values of the prefactors α and $\bar{\alpha}$ of the logarithmic renormalization of κ and $\bar{\kappa}$ — compare Eqs. (11) and (12), respectively:
  $\alpha = +3$, $\bar{\alpha} = 10/3$ (Peliti & Leibler 1985; Cai *et al.* 1994) [33, 34];
  $\alpha = +1$, $\bar{\alpha} = 0$ (Helfrich 1985) [48]
  $\alpha = -1$, $\bar{\alpha} = 0$ (Helfrich 1998) [49]
  The phase diagram of Fig. 9 has been calculated for $\alpha = +3$, $\bar{\alpha} = 10/3$. It looks very different for the other values given above.

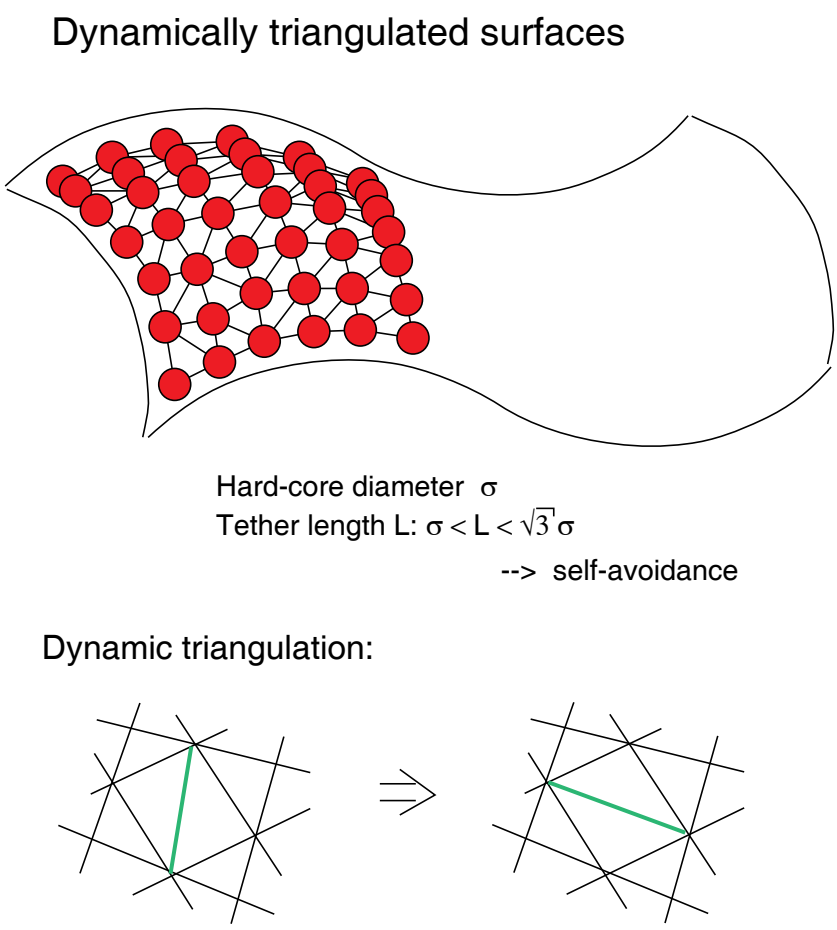

Fig. 12: *A triangulated network model of a fluctuating surface. Top: Hard spheres connected by bonds of maximum extension ℓ are used to describe self-avoiding membranes. Bottom: The Monte Carlo step, which makes the triangulation dynamic, is required to model fluid membranes.*

- The instability argument for the position of the phase transitions, as well as the other calculations which lead to the phase diagram of Fig. 9 apply for $\kappa \gg k_B T$. However, microemulsions and sponge phases typically occur in systems with small bending rigidities of $\kappa \simeq k_B T$.

- Sponge phases with random geometry and bicontinuous *cubic* phases with minimal surface structure cannot be distinguished in the "Fluctuating Membranes" approach. Therefore, few predictions are available from this approach for the structure of the bicontinuous phases.

Simulation method — The simulation of highly dilute sponge phases, with characteristic domain sizes on the order of 10-100nm is impossible on the basis of a molecular model, since it would require an enormous number of "solvent molecules". Therefore, the most appropriate model is again the random surface model discussed above. In order to make this model suitable for simulations, the continuous surface has to be approximated by a network of vertices and bonds, see Fig. 12. A triangular network is usually used because it provides the most homogeneous and isotropic discretization of the surface. A Monte Carlo step then consists of a

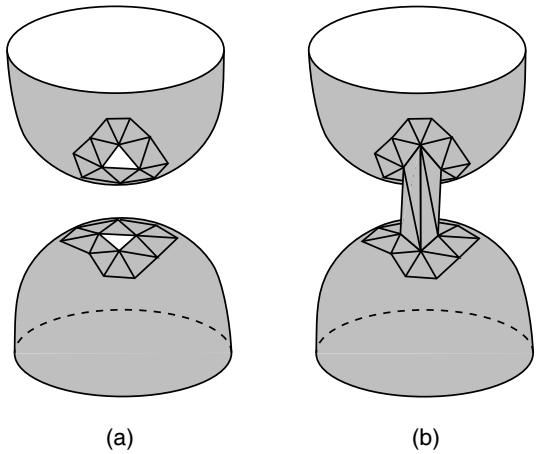

Fig. 13: *Schematic representation of the Monte Carlo step, which is used to change the topology of a randomly triangulated surface. For details see text.*

random displacement of a randomly selected vertex. This step is accepted with the probability determined by the Boltzmann weight, as long as the vertices remain within the maximum bond lengths with their neighbors. The energy, which appears in the Boltzmann weight is the curvature energy, which can be discretized in the form [50, 51]

$$E_b = \lambda_b \sum_{<ij>} (1 - \mathbf{n}_i \cdot \mathbf{n}_j) \tag{38}$$

where $\mathbf{n}_i$ and $\mathbf{n}_j$ are the normal vectors of neighboring triangles, and the sum runs over all pairs of neighboring triangles. The coupling constant λ_b in Eq. (38) is related to the bending rigidity and saddle-splay modulus by $\kappa = \sqrt{3}\lambda_b/2$ and $\bar{\kappa} = -4\kappa/3$ [52]. Other discretizations are discussed in Ref. [53].

Such a model has first been suggested and simulated for *polymerized membranes* by Kantor & Nelson (1987) [50, 51]. When hard spheres of diameter σ_0 are placed on the vertices, and the bond lengths ℓ are restricted to be $\ell \leq \sqrt{3}\sigma_0$, the surface is *self-avoiding*, since an arbitrary sphere does *not* fit through the holes of the network, so that no interpenetration of different parts of the network is possible.

For a study of fluid membranes, the connectivity of the membrane cannot remain fixed during the simulation, because otherwise a diffusion of vertices within the membrane is not possible. Therefore, dynamically triangulated surfaces [11, 54] have to be used in this case. The essential step of the dynamic triangulation procedure is shown at the bottom of Fig. 12. Among the four vertices of two neighboring triangles, the "diagonal" bond is switched from one of the two possible positions to the other. This bond-switching is only allowed if the vertices remain connected to at least three neighbors after the switch. Also, the distance between the newly connected vertices has to be smaller than the maximum bond length. This Monte Carlo step has the advantages that

- is is local, i.e. only the vertices of two neighboring triangles are involved, and
- it guarantees that the network retains its two-dimensional connectivity during the whole simulation run.

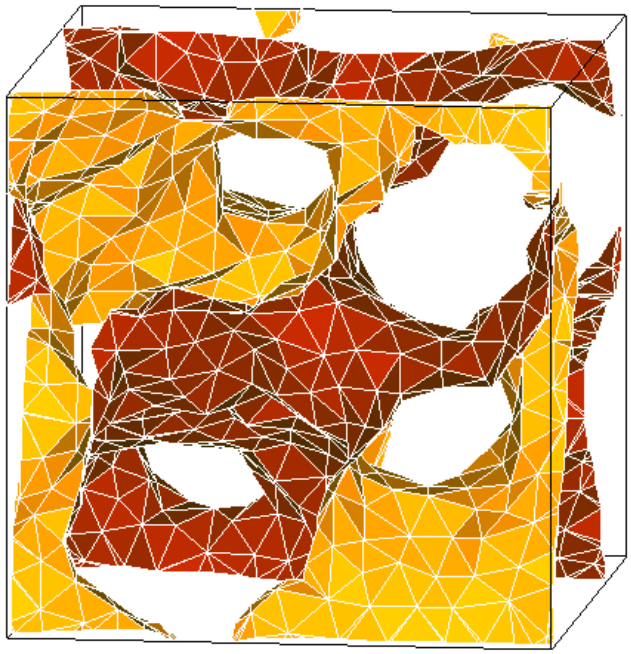

Fig. 14: *A typical conformation of the membrane in a sponge phase, as obtained from Monte Carlo simulations of randomly triangulated surfaces (Gompper & Kroll 1998) [55]. The two sides of the membrane are colored differently to emphasize the bicontinuous structure.*

Finally, in order to study membrane ensembles with fluctuating topology, a Monte Carlo step is required which changes the topology. Such a step is shown schematically in Fig. 13. It consists of removing two triangles from the network, which are located sufficiently closely in the embedding space that a prism of six new triangles can be inserted without exceeding the maximum bond lengths to form a passage-like connection between the previously disjoint membrane patches [55, 54]. Obviously, the inverse step is also possible, where a passage is removed and two triangles are inserted to close the holes in the network.

Simulation Results — A typical conformation of the membrane in the region of the parameter space, where the sponge phase is stable, is shown in Fig. 14. This configuration shows all the characteristic features of a sponge phase, which have been discussed above, such as the bicontinuous structure and the local saddle-like shape of the membrane.

A more quantitative analysis is possible by calculating thermal averages for many different values of the parameters, and then constructing a phase diagram, as shown in Fig. 15. The Monte Carlo data [55] for the phase boundaries are found to follow the logarithmic dependence expected from Eq. (16). Furthermore, the slopes of these phase boundaries in a semi-logarithmic plot are quite consistent with the $\bar{\alpha} = 10/3$, while $\bar{\alpha} = 0$ can clearly be ruled out. Thus, the Monte Carlo results strongly support the "Fluctuating Membranes" predictions, with the value of $\bar{\alpha}$ predicted in Refs. [33, 34].

Another quantity, which can be obtained from the simulations and compared directly with the analytical predictions is the osmotic pressure p . In the analytical approaches, it is obtained

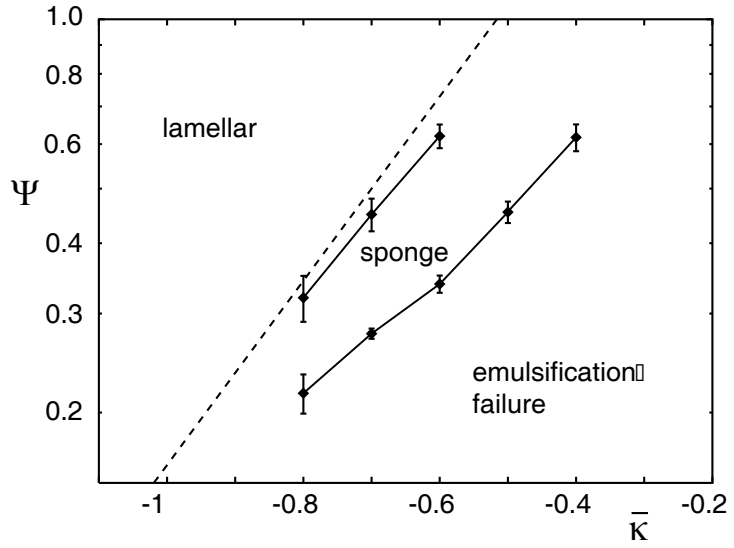

Fig. 15: *Phase diagram of random surfaces controlled by curvature elasticity, as obtained from Monte Carlo simulations of randomly triangulated surfaces with $\kappa \simeq 1.7 k_B T$ (Gompper & Kroll 1998) [55]. The dashed line shows the theoretical prediction (16), with $\bar{\alpha} = 10/3$.*

from the free-energy density f by differentiation,

$$\begin{aligned} \frac{p}{k_B T} &= \Psi \frac{\partial f}{\partial \Psi} - f \\ &= [A'' + B'' \ln(\Psi)] \Psi^3 \qquad \text{(fluctuating membranes)} \end{aligned} \tag{39}$$

and in the case of the free-energy density (36) has the same functional form as f itself. The simulation results (Gompper & Kroll 1998) [55] are compared with this prediction in Fig. 16. Again, the simulation results are in very good agreement with the "Fluctuating Membranes" prediction.

Bulk scattering curves for three different membrane volume fractions Ψ are shown in Fig. 17. The peak position k_0 moves out and the peak broadens, roughly linearly with the membrane volume fractions Ψ, as expected from the variational GRF model, compare Eq. (35). However, the dimensionless length-scale rate $k_0 \xi$ is *not* independent of Ψ, in contrast to the GRF prediction.

5 Experimental Results

Phase behavior of binary systems — The elastic properties of an amphiphilic bilayer can be rather easily related to the elastic properties of the two monolayers of which the bilayer is composed (Petrov et al. 1978, Porte 1989) [57, 58]. This is done by writing the bilayer energy of a spherical cap as

$$\begin{aligned} E_b = \int dS \quad & \left\{ \left[2\kappa \left(\frac{1}{R+\epsilon} + c_0 \right)^2 + \bar{\kappa} \frac{1}{(R+\epsilon)^2} \right] \frac{(R+\epsilon)^2}{R^2} \right. \\ & \left. + \left[2\kappa \left(\frac{1}{R-\epsilon} - c_0 \right)^2 + \bar{\kappa} \frac{1}{(R-\epsilon)^2} \right] \frac{(R-\epsilon)^2}{R^2} \right\} \end{aligned} \tag{40}$$

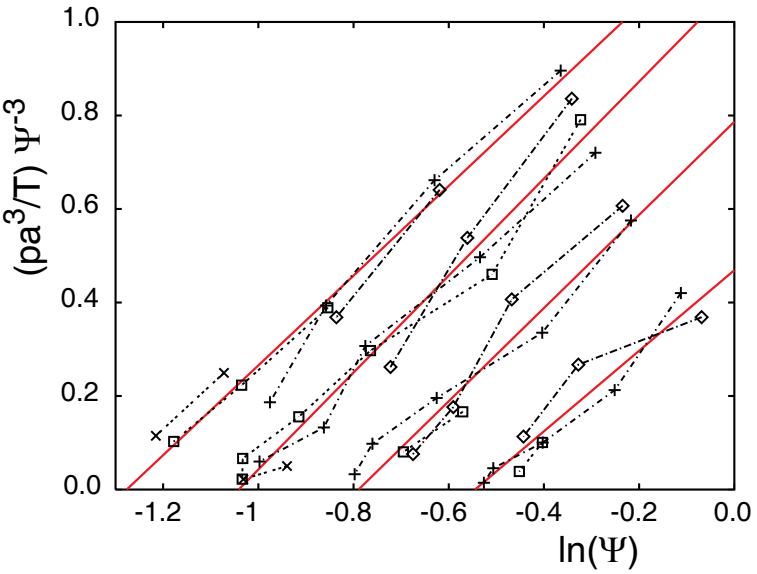

Fig. 16: *Scaled osmotic pressure* $(pa^3/k_BT)\Psi^{-3}$ *of random surfaces controlled by curvature elasticity, as obtained from Monte Carlo simulations of randomly triangulated surfaces for* $\kappa \simeq 1.0k_BT$ *(Gompper & Kroll 1998) [55]. Here,* a *is the membrane thickness. Data sets from right to left correspond to* $\bar{\kappa} = -0.4k_BT$, $\bar{\kappa} = -0.5k_BT$, $\bar{\kappa} = -0.6k_BT$ *and* $\bar{\kappa} = -0.7k_BT$. *The solid red lines indicate the theoretical prediction (36).*

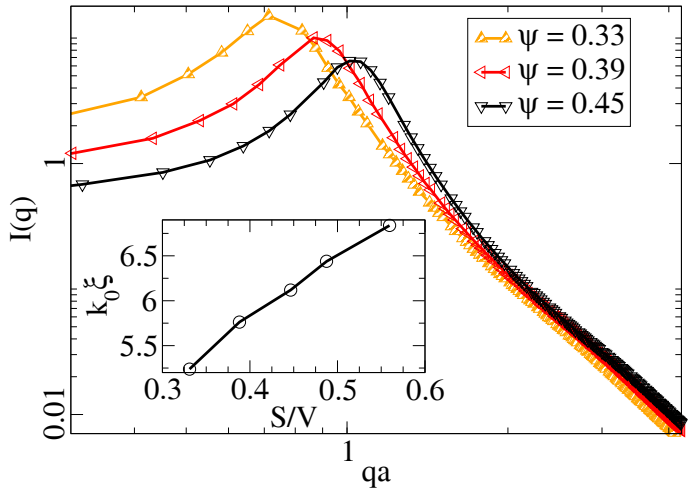

Fig. 17: *Bulk scattering intensity for three membrane volume fractions* $\Psi = aS/V$ *(see legend), as obtained Monte Carlo simulations for* $\kappa \simeq 3.5k_BT$ *and* $\bar{\kappa} = -0.6k_BT$. *The inset shows the length-scale ratio* $k_0\xi$ *as a function of* S/V. *From Peltomäki et al. (2012) [56].*

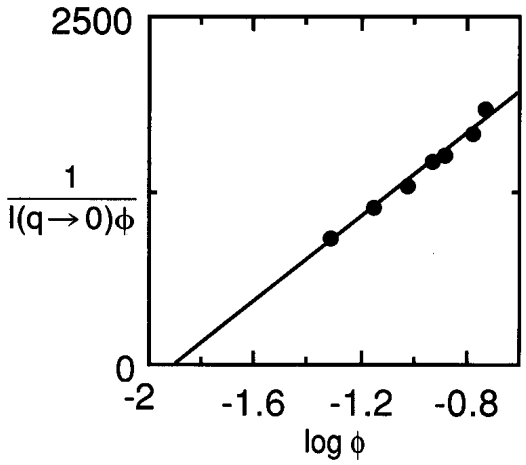

Fig. 18: *Experimental results for the film scattering intensity $I(q)$ in the limit of zero wave vector* $\mathbf{q}$ *in the system AOT–water–$NaCl$ (Skouri et al. 1991) [60].*

where R is the radius of curvature of the bilayer midsurface, ϵ is the thickness of a monolayer, and the integral extends over the surface of the midplane. The expansion of this expression in powers of $1/R$, together with a similar expansion of the energy of a cylindrical or saddle-shaped surface, gives again the form of the curvature energy, but now with

$$c_0^{(bi)} = 0 \quad , \quad \kappa^{(bi)} = 2\kappa \quad , \quad \bar{\kappa}^{(bi)} = 2\bar{\kappa} + 8\kappa c_0 \epsilon \tag{41}$$

Thus, the spontaneous curvature of a bilayer vanishes due to symmetry, but its saddle-splay modulus is related to the spontaneous curvature of the monolayers.
Now, the spontaneous curvature of monolayer has been shown experimentally (Strey 1994) [59] in ternary microemulsions to follow a linear temperature dependence

$$c_0^{(mono)} \sim (T - \bar{T}) \tag{42}$$

over a wide range of temperatures, where $\bar{T}$ is the hydrophobic-hydrophilic-balance temperature, which corresponds to balanced microemulsions. Therefore, $\bar{\kappa}^{(bi)} \sim (T - T^*)$, where T^* is a constant, and we expect the lamellar-to-sponge and the emulsification failure phase transitions to follow the relation

$$\ln(\Psi) \sim (T - T^*) \tag{43}$$

which corresponds to a straight line in a semi-logarithmic representation of the phase diagram. The experimental phase diagram is indeed consistent with such a behavior, as can be seen from Fig. 3.

Small-Angle Scattering — In the limit of very small wave vectors q, the scattering intensity in *film contrast* is determined by the osmotic compressibility, so that [32]

$$\begin{aligned} I(q \to 0) &= \Psi \left(\frac{\partial p}{\partial \Psi} \right)^{-1} \\ &\sim \Psi^{-1} [A''' + B''' \ln(\Psi)]^{-1} \quad \text{(fluctuating membranes)} \end{aligned} \tag{44}$$

This expression is compared to experimental data [32, 60] for the system AOT–water–$NaCl$ in Fig. 18. The data nicely agree with the behavior predicted behavior for "Fluctuating Membranes".

6 Beyond "Simple" Amphiphilic Systems

6.1 Amphiphilic Block Copolymers in Ternary Mixtures

Fig. 19: *Effect of small amounts of amphiphilic block copolymer PEP-PEO (compare Fig. 21 below) on the phase behavior of balanced microemulsions. Far left: oil-water coexistence. Left: 7 weight % surfactant $C_{10}E_4$ produce a three-phase coexistence with a microemulsion phase in the center. Right: 0.5 weight % of PEP*5*-PEO*5 *increase the microemulsion volume two-fold. Far right: 1.0 weight % of PEP*5*-PEO*5 *increases the microemulsion volume three-fold (preparation and photo: J. Allgaier).*

It has been found very recently that the addition of small amounts of amphiphilic block copolymers to balanced microemulsions has a dramatic effect on the phase behavior (Jakobs et al. 1999) [61]. As shown in Fig. 19, the ability of a short-chain surfactant to solubilize oil and water into a macroscopically homogeneous and isotropic microemulsion phase increases dramatically when a small percentage of the total surfactant weight is added as amphiphilic block copolymer. The block copolymer used in this study is polyethyleneoxide–polyethylenepropylene PEOx-PEPy, where x and y denote the molecular weights of each block in kg/mol. The chemical structure of the polymers mimics the structure of the non-ionic C_iE_j surfactant, and PEP10-PEO10 corresponds roughly to $C_{715}E_{230}$. Note that while the microemulsion is completely transparent without block copolymer, it becomes more and more opaque with increasing block-copolymer concentration. This indicates that the scale of the oil- and water domains is increasing with increasing block-copolymer concentration, and it approaches the wavelength of light at the highest polymer concentrations in Fig. 19.

A typical conformation of a polymer-decorated membrane is shown in Fig. 20 on the mesoscopic scale. The block copolymers are incorporated into the surfactant-monolayer membrane, such that the hydrophilic block is located in the water domains, while the hydrophobic block is in the oil domains.

The dramatic effect of amphiphilic block copolymers on the microemulsion can be understood on the basis of the membrane-curvature model [63, 64, 65]. Polymer chains anchored to a

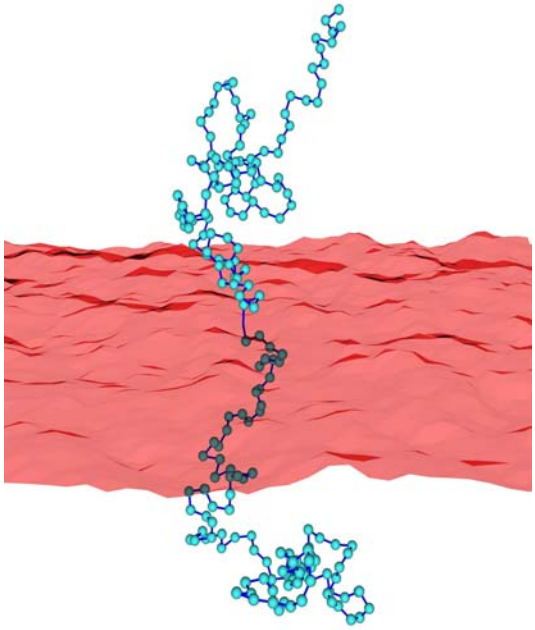

Fig. 20: *Typical conformation of a polymer-decorated membrane (Auth & Gompper 2003) [62]. For details see text.*

membrane modify the curvature elasticity such that (Hiergeist & Lipowsky 1996, Eisenriegler et al. 1996, Auth & Gompper 2003) [66, 67, 62]

$$\kappa_{eff} = \kappa + \frac{k_B T}{12}\left(1+\frac{\pi}{2}\right)\sigma(R_w^2+R_o^2) \tag{45}$$

$$\bar{\kappa}_{eff} = \bar{\kappa} - \frac{k_B T}{6}\sigma(R_w^2+R_o^2) \tag{46}$$

where σ is the grafting density of the polymer, i.e. the number of polymer anchoring points per unit membrane area, and R_w^2 and R_o^2 are the mean-squared end-to-end distances of the polymer blocks in the water- and oil-domains, respectively (compare Fig. 21). Eqs. (45) and (46) apply in the so-called mushroom regime, where the polymer density on the membrane is so small that the polymer coils do not interact directly with each other. Thus, the bending rigidity and the saddle-splay modulus increase *linearly* with the scaled polymer grafting density $\sigma(R_o^2+R_w^2)$ in this regime. It should be noticed that this is a very *small effect*, since even at the overlap concentration, where $\sigma(R_o^2+R_w^2)=2$ for a symmetric block copolymer, the increment of κ and $|\bar{\kappa}|$ is only a fraction of k_BT. The results (45) and (46) can be compared, for example, with the elastic properties of solid elastic sheets, where the bending rigidity scales with the sheet thickness ℓ_0 as $\kappa \sim \ell_0^3$ [68].

The increase of the effective bending rigidity κ_{eff} in Eq. (45) and of the magnitude of $\bar{\kappa}_{eff}$ in Eq. (46) can be understood from the entropy loss of each polymer coil in a confined geometry due to the restriction of the number of accessible configurations. This entropic repulsion suppresses membrane fluctuations *and* disfavors saddle-like conformations near the anchoring points. A simple, heuristic argument for the suppression of saddle-like conformations has been given by Milner & Witten (1988) [69] for polymers in the brush regime, where there is a strong

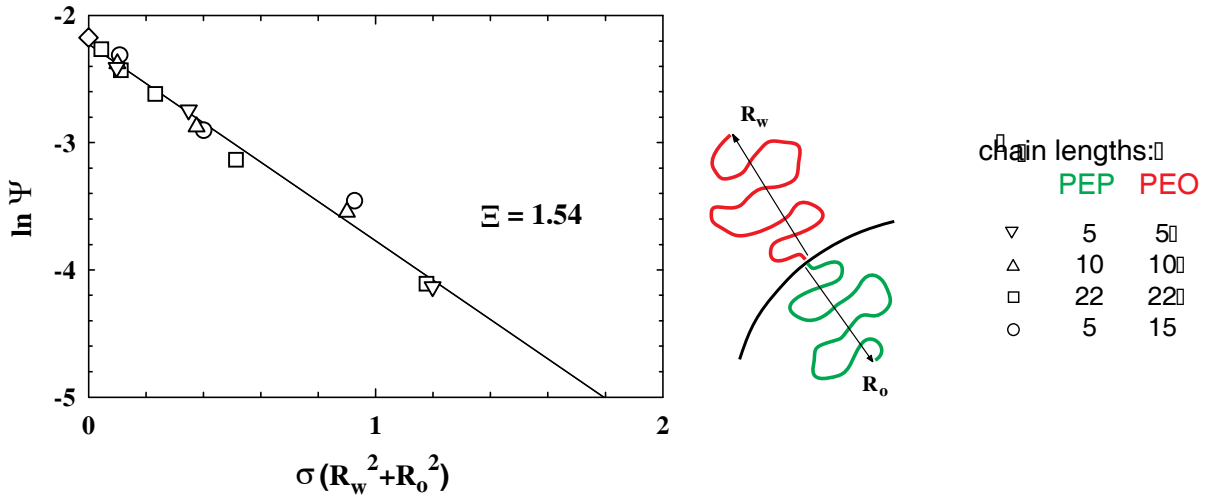

Fig. 21: *Phase diagram of a microemulsion of water–decane–$C_{10}E_4$ with amphiphilic block copolymer. The membrane volume fraction Ψ of the microemulsion at three-phase coexistence is shown as a function of the scaled polymer grafting density on the membrane (Endo et al. 2000) [63]. The different symbols correspond to different molecular weights (in kg/mol) of the four different PEP-PEO block copolymers. Average end-to-end distances of the two blocks in the water and oil subphase are denoted by R_w and R_o, respectively.*

overlap between neighboring chains on the membrane. Consider the volume V of a thin shell of thickness ℓ_0 above a surface of area A bent with local curvatures c_1 and c_2. The ratio $V/(A\ell_0)$ is the ratio of volume available for chains in a layer of thickness ℓ_0 and grafting area A in the bent and unbent geometries, and may be expanded as

$$\frac{V}{A\ell_0} = 1 + H\ell_0 + \frac{1}{3}K\ell_0^2 + ... \tag{47}$$

where H and K are the mean and Gaussian curvatures, respectively. This relation can be checked easily for a spherical and a cylindrical surface. Then for a saddle surface, $H = 0$ and $K = -1/R^2$, so that $V/(A\ell_0) \simeq 1 - \frac{1}{3}(\ell_0/R)^2$; the bent thin shells have therefore *less space* available for monomers than the unbent shells, and the polymer chains must stretch upon bending, which costs free energy. The same argument should also apply to the mushroom regime.

Thus, from the combination of Eqs. (16) and (46), the prediction

$$\begin{aligned} \ln(\Psi/\Psi^*) &= \frac{4\pi}{\bar{\alpha}}\frac{1}{6}\sigma(R_w^2 + R_o^2) \\ &= -\frac{\pi}{5}\sigma(R_w^2 + R_o^2) \end{aligned} \tag{48}$$

for the dependence of the emulsification boundary on the scaled polymer density is obtained. This result is compared with experimental data for a number of different block-copolymer lengths in Fig. 21. The exponential dependence of the membrane volume fraction Ψ at three-phase coexistence is very nicely confirmed. In fact, this *exponential* dependence is responsible that the small increment in the magnitude of the saddle-splay modulus has the dramatic effects on the phase behavior shown in Fig. 19. Also, the data for different polymer lengths scale exactly as predicted by Eq. (48). A fit of the experimental data in Fig. 21 to the functional form

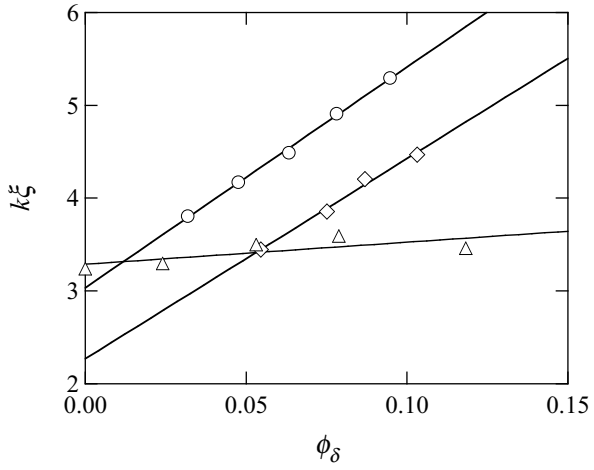

Fig. 22: *Dimensionless ratio $k_0\xi$ of the two characteristic length scales of a microemulsion, as a function of the polymer content, ϕ_δ, in the mixture of both amphiphiles, which is proportional to the polymer grafting density on the membrane (Gompper et al. 2001) [70]. The two data sets marked by circles ($\circ$) and diamonds ($\diamond$) were obtained for PEP5-PEO5 at fixed membrane volume fractions of $\Psi = 0.12$ and $\Psi = 0.08$, respectively. The data set marked by triangles ($\triangle$) were taken for PEP10-PEO10 along three-phase coexistence.*

of Eq. (48) yields a prefactor $\Xi = 1.54$, which is a bit more than a factor two larger than the theoretical result $\pi/5 \simeq 0.628$. A possible reason for this discrepancy is the theoretical result (45) has been obtained for ideal chains, while the polymer chains are self-avoiding in the real system. This is one of the few examples, where a *quantitative* comparison of experimental data and theoretical results has been achieved for these complex, disordered, and mesoscopically structured fluid phases.

It is possible to go one step further and also investigate the scattering behavior [70]. In this case, the Monte Carlo simulations of triangulated surfaces predicts (Peltomäki et al. 2012) [56],

$$k_0\xi = 7.39(0.15\kappa^R + 0.85\bar{\kappa}^R) \sim \sigma(R_o^2 + R_w^2) \tag{49}$$

where the later relation follows from Eqs. (45) and (46). The experimental data for this characteristic number are shown in Fig. 22. The data for fixed surfactant concentration, i.e. for fixed membrane area, follow precisely the behavior of Eq. (49). It is important to notice, however, that although the lines have equal slope, as expected from Eq. (49), they are shifted relative to each other. The data along the coexistence line still depend linearly on the polymer content ϕ_δ in the mixture of both amphiphiles, but even the slope is different. This is due to the logarithmic renormalization of the bending rigidity [70, 56].

The extraction of bending rigidities has been applied recently to other microemulsion systems, in particular to microemulsions containing supercritical CO_2 instead of oil [71, 72].

6.2 Interfaces and Walls

So far, we have focused on bulk phases. However, microemulsions can of course coexist with other phases, such as a water-rich and an oil-rich phase, see Sec. 2. Particularly important is also the behavior near wall, because microemulsions are used, for example, for cleaning processes.

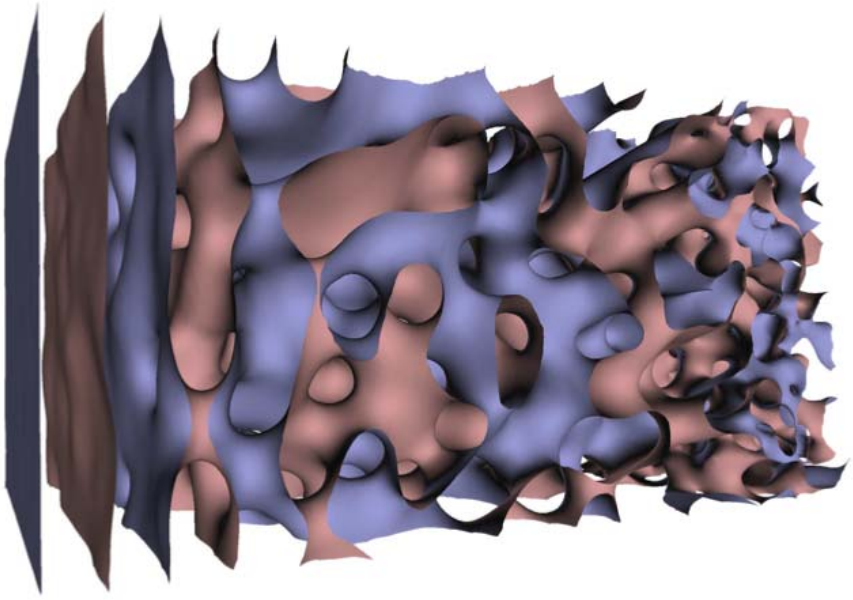

Fig. 23: *Microemulsion near a planar wall (left). The wall induces a lamellar structure close to it (Kerscher et al. 2011) [73].*

Results of Monte Carlo simulations employing the Ginzburg-Landau model described in Sec. 3.3 for the microemulsion structure near a wall shown in Fig. 23. The planar wall induces a few layers of the lamellar phase near the wall. The scattering intensity for a small angle neutron scattering study under grazing incidence (GISANS) , which is predicted from this structure, agrees very well the recent experimental results (Kerscher et al. 2011) [73]. An interesting theoretical prediction is that the "transition" from perfect lamellae to the bicontinuous structure occurs through a layer of perforated lamellae, where neighboring membranes are connected by catenoid-like passages.
Another interesting interface occurs between different domains of the same phase of ordered bicontinuous structure, which are well described by triply periodic minimal surfaces, compare Sec. 3.2. As for any other crystalline material, different kind of interfaces can be distinguished, in particular tilt and twist grain boundaries, where the two grains are rotated with respect to each other with a rotation axis parallel and perpendicular to the interface, respectively. Results of a free-energy minimization in the Ginzburg-Landau model are show in Fig. 24. The interface is difficult to see, because the membrane structure adapts to the constraints very well. This makes it plausible that also the interface energy (corresponding to the surface tension between fluid interfaces) is very small, which is indeed the result of the calculation [74]. This implies that grain boundaries should be easily excited by external forces.

7 Summary and Conclusions

Research in the field of Soft Matter systems is an interdisciplinary endeavor. The work on random surfaces and fluctuating membranes brings together mathematicians (minimal surfaces), theoretical physicists (statistical physics, field theory), experimental physicists (neutron scat-

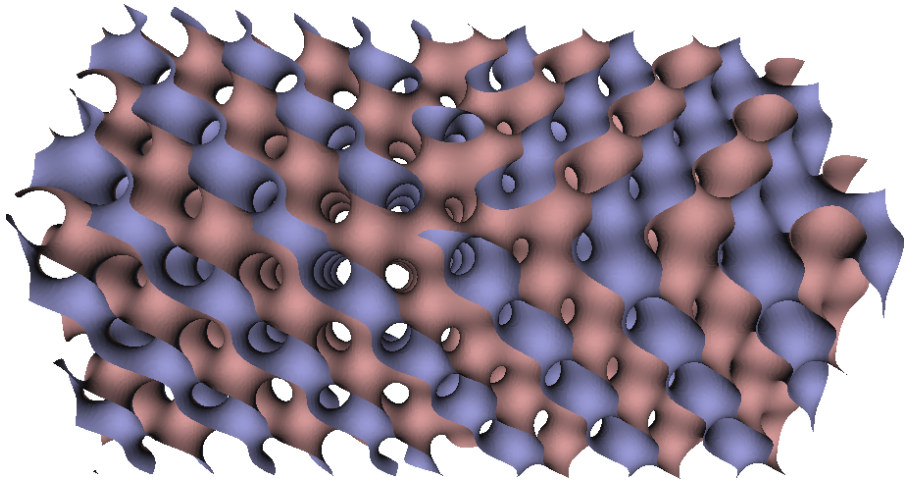

Fig. 24: *Interface between two different domains of the gyroid phase. The interface, a twist grain boundary, is vertical, with the domains of the TPMS to the left and right, rotated by an angle of* 90^o *with respect to each other (Belushkin & Gompper 2009) [74].*

tering, microscopy), chemists (synthesis, phase behavior), biologists (cell membranes), and material scientists (nanoscale materials).

Over the last twenty years, the joint effort of researches from these different disciplines has lead to significant progress in our understanding of amphiphilic systems. For the "simple" system of an ensemble of membranes without internal structure, the qualitative behavior is reasonably well understood. On the quantitative level, there remains still a lot of work to be done. As the discussion of the previous sections has demonstrated, the results of different approximate approaches do not always agree. Also, experiments are often done in rather complex systems, where several different physical mechanisms are at work simultaneously, which make the interpretation of the results difficult. Therefore, even the "simple" system will require much more work before a satisfactory level of understanding has been reached.

The comparison of theoretical models, computer simulation results, and experimental data indicates that the "fluctuating interfaces" approach works very well. The effect of the logarithmic renormalization of the elastic curvature moduli now seems to be well established. Simulations show that also scattering intensities of microemulsion or sponge phases can be predicted from this approach. The results are predicted surprisingly well by the "Gaussian random field" approach, but show important qualitative and quantitative differences.

In the recent past, and undoubtedly in the future, the trend will go towards more complex systems. With the increasing number of components, the system will become more flexible, with properties which can be controlled and manipulated externally. Here, the contact with biology will certainly intensify. For Statistical Physics, it will be a very interesting task to predict the properties of such complex systems quantitatively.

Appendices

A Correlation Functions of Gaussian Free-Energy Functionals

The partition function Z for any free-energy functional $\mathcal{F}(\Phi)$ is a functional integral over all order parameter configurations $\Phi(\mathbf{r})$. This integral is written formally as

$$Z_0 = \int \mathcal{D}\Phi \exp[-\mathcal{F}] \tag{50}$$

By adding auxiliary fields $H(\mathbf{r}$ to the free-energy functional, correlation functions can be derived from the (modified) partition function

$$Z\{H\} = \int \mathcal{D}\Phi \exp\left[-\mathcal{F} + \int d^3r H(\mathbf{r})\Phi(\mathbf{r})\right] \tag{51}$$

by functional differentiation. For example, the two-point order parameter correlation function is obtained as

$$G(\mathbf{r}-\mathbf{r}') =< \Phi(\mathbf{r})\Phi(\mathbf{r}') >= \frac{1}{Z_0}\frac{\delta^2 Z\{H\}}{\delta H(\mathbf{r})\delta H(\mathbf{r}')}|_{H=0}\,. \tag{52}$$

The exact evaluation of the functional integral (51) is, however, only possible in a few special cases; in particular, this is possible for free-energy functionals of the quadratic form

$$\mathcal{F}_0 = \int d^3r \int d^3r'\, w(|\mathbf{r}-\mathbf{r}'|)\Phi(\mathbf{r})\Phi(\mathbf{r}') \tag{53}$$

$$= \int d^3q\, w(|\mathbf{q}|)\Phi(\mathbf{q})\Phi(-\mathbf{q}) \tag{54}$$

For the free-energy functional of Eq. (19), a Fourier transformation yields

$$w(q) = \frac{1}{2}\left(c_0 q^4 + b_0 q^2 + a_0\right) \tag{55}$$

In all other cases of non-Gaussian functionals, one has to resort to a perturbative approach [75, 44].

We want to focus here on the calculation of correlation functions. For the functional (53), the partition function (51) is given by

$$Z\{H\} = \int \mathcal{D}\Phi\, \exp\left[\int d^3q\,[-w(|\mathbf{q}|)\Phi(\mathbf{q})\Phi(-\mathbf{q}) + H(\mathbf{q})\Phi(-\mathbf{q})]\right] \tag{56}$$

By completing the square in the exponent, we obtain

$$Z\{H\} = \int \mathcal{D}\Phi\, \exp\left[\int d^3q \left[-w(q)\left|\left(\Phi(\mathbf{q}) - \frac{H(\mathbf{q})}{2w(q)}\right)\right|^2 - \frac{H(\mathbf{q})H(-\mathbf{q})}{4w(q)}\right]\right] \tag{57}$$

Here, we have used that the order parameter $\Phi(\mathbf{r})$ and the auxiliary fields $H(\mathbf{r})$ are real numbers, so that $\Phi(-\mathbf{q}) = \Phi(\mathbf{q})^*$ and $H(-\mathbf{q}) = H(\mathbf{q})^*$. By introducing the new integration variables $\tilde{\Phi}(\mathbf{q}) = \Phi(\mathbf{q}) - H(\mathbf{q})/2w(q)$, we obtain from Eq. (57)

$$Z\{H\} = \exp\left[-\frac{H(\mathbf{q})H(-\mathbf{q})}{4w(q)}\right] \int \mathcal{D}\tilde{\Phi}\, \exp\left[-\int d^3q\, w(q)\tilde{\Phi}(\mathbf{q})\tilde{\Phi}(-\mathbf{q})\right] \tag{58}$$

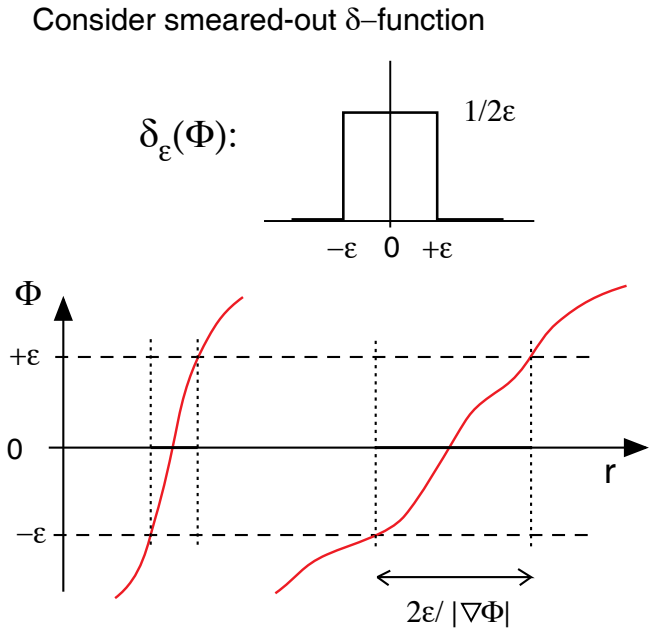

Fig. 25: *In order to calculate the surface area of level surfaces of Gaussian random fields, the δ-function in Φ has to be corrected for the different local gradients of the order-parameter field. For details see text.*

The remaining functional integral is the partition function Z_0, compare Eq. (50), which is *independent* of the fields $H(\mathbf{q})$, and therefore is not required for the calculation of correlation functions. The evaluation of the functional derivatives in Eq. (52) is now straightforward and yields

$$G(\mathbf{q}) = \frac{1}{2w(q)} \tag{59}$$

Together with Eq. (55), this implies Eq. (20).

B Calculation of the Surface Density S/V for Gaussian Random Fields

We briefly sketch the calculation of the surface density S/V for Gaussian random. It is clear that the surface density must be related to the average of $\delta(\Phi(\mathbf{r})-\alpha)$. However, note that in contrast to the particle density of molecules or colloidal particles, which is given by $\rho(\mathbf{r}) = \sum_i \delta(\mathbf{r}-\mathbf{r}_i)$, the δ-function for the level surfaces acts on the Φ-variable, rather than the space variable $\mathbf{r}$ is in the usual case. Therefore, we need the mathematical identity

$$\delta(\Phi(\mathbf{r}) - \alpha) = \frac{1}{|\nabla\Phi(\mathbf{r})|}\delta(\mathbf{r} - \mathbf{r}_0) \tag{60}$$

where $\mathbf{r}_0$ is the location of the level surface. The surface density is therefore given by

$$S/V = \langle |\nabla\Phi(\mathbf{r})|\, \delta(\Phi(\mathbf{r}) - \alpha)\rangle \tag{61}$$

There is another, more intuitive way to arrive at the same conclusion. Let us consider a smeared-out δ-function of width ϵ, as shown in Fig. 25 (upper part). The contribution to the average of the function δ_ϵ now clearly depends on the gradient of Φ; if the gradient is small (large), the contribution is large (small), as shown in Fig. 25 (lower part). Since for the calculation of S/V the contribution of all parts of the surface must be the same — independent of the local gradient of Φ — this effect has to be divided out, which gives again Eq. (61).
In order to calculate the average (61), we need the joint probability distribution function

$$P[\Phi(\mathbf{r}) = \alpha, \nabla\Phi(\mathbf{r}) = \mathbf{v}] = \langle \delta(\Phi(\mathbf{r}) - \alpha)\, \delta(\nabla\Phi(\mathbf{r}) - \mathbf{v}) \rangle \tag{62}$$

It is shown in detail in Appendix C that

$$P[\alpha, \mathbf{v}] = P_0 \exp\left[-\frac{\alpha^2}{2} - \frac{v^2}{2\sigma_v^2} \right] \tag{63}$$

with

$$\sigma_v = \frac{1}{3} \int \frac{d^3q}{(2\pi)^3}\, q^2 \nu(q) \equiv \frac{1}{3} \langle q^2 \rangle_\nu \tag{64}$$

and normalization

$$P_0 = (2\pi)^{-2} \sigma_v^{-3} \tag{65}$$

This implies

$$\begin{aligned} S/V &= \int d^3v |v| P(\alpha, \mathbf{v}) \\ &= 4\pi P_0 \int_0^\infty dv v^3 \exp[-\alpha^2/2 - v^2/(2\sigma_v^2)] \\ &= \frac{2}{\pi} \exp[-\alpha^2/2] \sqrt{\frac{1}{3}\langle q^2 \rangle_\nu} \end{aligned} \tag{66}$$

This is just the result (26).

C Joint Distribution of Gaussian Random Fields

Joint probability distribution functions are required for the calculation of geometrical averages of level surfaces of Gaussian random fields, see Appendix B. First, the probability distribution

$$P[\Phi(\mathbf{r}) = \alpha, \nabla\Phi(\mathbf{r}) = \mathbf{v}] = \langle \delta(\Phi(\mathbf{r}) - \alpha)\, \delta(\nabla\Phi(\mathbf{r}) - \mathbf{v}) \rangle \tag{67}$$

has to be calculated [39, 6]. Since this probability distribution only contains a single spatial variable, and the system is homogeneous on average, $\mathbf{r} = 0$ can be chosen without loss of generality. The representation

$$\delta(x) = \int_{-\infty}^{\infty} \frac{dk}{2\pi} \exp(ikx) \tag{68}$$

can now be used to obtain

$$P[\alpha, \mathbf{v}] = \int \frac{d\omega}{2\pi} \int \frac{d^3k}{(2\pi)^3} \left\langle e^{i\omega(\Phi(\mathbf{r}) - \alpha)} e^{i\mathbf{k}\cdot(\nabla\Phi(\mathbf{r}) - \mathbf{v})} \right\rangle \tag{69}$$

With the Fourier-representation

$$\Phi(\mathbf{r}) = \int \frac{d^3k}{(2\pi)^3}\Phi(\mathbf{q})e^{i\mathbf{q}\cdot\mathbf{r}} \tag{70}$$

this becomes

$$P[\alpha,\mathbf{v}] = \int \frac{d\omega}{2\pi}\int \frac{d^3k}{(2\pi)^3}e^{-i\omega\alpha - i\mathbf{k}\cdot\mathbf{v}}\left\langle \exp\int \frac{d^3q}{(2\pi)^3}[i\omega\Phi(\mathbf{q}) - \mathbf{k}\cdot\mathbf{q}\Phi(\mathbf{q})]\right\rangle \tag{71}$$

at $\mathbf{r} = 0$. The average in Eq. (71) has to be evaluated with the Boltzmann weight

$$\exp[-\mathcal{H}_0] = \exp\left\{-\frac{1}{2}\int \frac{d^3q}{(2\pi)^3}\nu(q)^{-1}|\Phi(\mathbf{q})|^2\right\} \tag{72}$$

which implies in particular

$$\langle\Phi(\mathbf{q})\Phi(\mathbf{q}')\rangle = \nu(q)(2\pi)^3\delta(\mathbf{q}+\mathbf{q}') \tag{73}$$

For a Gaussian-distributed variable $x \in \mathbb{C}$, the relation

$$\langle e^{ikx}\rangle = \exp(-\frac{1}{2}k^2\langle x^2\rangle) \tag{74}$$

holds exactly. Therefore,

$$\begin{aligned}
&\left\langle \exp\int \frac{d^3q}{(2\pi)^3}[i\omega - \mathbf{k}\cdot\mathbf{q}]\Phi(\mathbf{q})\right\rangle \\
&= \exp\left[\frac{1}{2}\int \frac{d^3q}{(2\pi)^3}\int \frac{d^3q'}{(2\pi)^3}(i\omega - \mathbf{k}\cdot\mathbf{q})(i\omega - \mathbf{k}\cdot\mathbf{q}')\langle\Phi(\mathbf{q})\Phi(\mathbf{q}')\rangle\right] \\
&= \exp\left[-\frac{1}{2}\int \frac{d^3q}{(2\pi)^3}(\omega^2 + (\mathbf{k}\cdot\mathbf{q})^2)\nu(q)\right]
\end{aligned} \tag{75}$$

so that

$$P[\alpha,\mathbf{v}] = \int \frac{d\omega}{2\pi}\int \frac{d^3k}{(2\pi)^3}e^{-i\omega\alpha - i\mathbf{k}\cdot\mathbf{v}}\exp\int \frac{d^3q}{(2\pi)^3}\left[-\frac{1}{2}\omega^2 - \frac{1}{2}(\mathbf{k}\cdot\mathbf{q})^2\right]\nu(q) \tag{76}$$

The remaining integrals are now straightforward. In particular,

$$\int \frac{d^3q}{(2\pi)^3}(\mathbf{k}\cdot\mathbf{q})^2\,\nu(q) = \frac{1}{3}k^2\langle q^2\rangle_\nu \equiv k^2\sigma_v^2 \tag{77}$$

with $\langle ...\rangle_\nu$ defined in Eq. (30), and

$$\int \frac{d^3k}{(2\pi)^3}e^{-i\mathbf{k}\cdot\mathbf{v}}\,e^{-\frac{1}{6}k^2\langle q^2\rangle} = (2\pi)^{-3/2}\sigma_v^{-3}\exp\left[-\frac{1}{2}\frac{v^2}{\sigma_v^2}\right] \tag{78}$$

References

[1] Research in Jülich, Nr. 2/2006, Physics meets Biology.

[2] G. Gompper, J. K. G. Dhont, and D. Richter, Eur. Phys. J. E **26**, 1 (2008).

[3] G. Porte, J. Phys.: Condens. Matter **4**, 8649 (1992).

[4] G. Gompper and M. Schick, in *Phase Transitions and Critical Phenomena*, edited by C. Domb and J. Lebowitz (Academic Press, London, 1994), vol. 16, pp. 1–176.

[5] W. M. Gelbart, A. Ben-Shaul, and D. Roux, eds., *Micelles, Membranes, Microemulsions, and Monolayers* (Springer-Verlag, Berlin, 1994).

[6] S. A. Safran, *Statistical Thermodynamics of Surfaces, Interfaces, and Membranes* (Addison-Wesley, Reading, MA, 1994).

[7] D. F. Evans and H. Wennerström, *The Colloidal Domain, where Physics, Chemistry, Biology and Technology Meet* (VCH Publishers, New York, 1994).

[8] R. Lipowsky and E. Sackmann, eds., *Structure and dynamics of membranes - from cells to vesicles*, vol. 1 of *Handbook of biological physics* (Elsevier, Amsterdam, 1995).

[9] F. David, P. Ginsparg, and J. Zinn-Justin, eds., *Fluctuating geometries in statistical mechanics and field theory* (Elsevier, Amsterdam, 1996).

[10] U. Seifert, Adv. Phys. **46**, 13 (1997).

[11] G. Gompper and D. M. Kroll, J. Phys.: Condens. Matter **9**, 8795 (1997).

[12] M. E. Cates and M. R. Evans, *Soft and Fragile Matter: Nonequilibrium Dynamics, Metastability and Flow* (Institute of Physics, London, 2000).

[13] J. K. G. Dhont, G. Gompper, and D. Richter, eds., *Soft Matter — Complex Materials on Mesoscopic Scales*, vol. 10 of *Matter and Materials* (Forschungszentrum Jülich, Jülich, 2002).

[14] D. Nelson, T. Piran, and S. Weinberg, eds., *Statistical Mechanics of Membranes and Surfaces* (World Scientific, Singapore, 2004), 2nd ed.

[15] T. A. Witten and P. A. Pincus, *Structured Fluids: Polymers, Colloids, Surfactants* (Oxford University Press, Oxford, 2006).

[16] W. C. K. Poon and D. Andelman, *Soft Condensed Matter Physics in Molecular and Cell Biology* (Taylor & Francis, Boca Raton, 2006).

[17] J. K. G. Dhont, G. Gompper, G. Nägele, D. Richter, and R. G. Winkler, eds., *Soft Matter — From Synthetic to Biological Materials*, vol. 1 of *Key Technologies* (Forschungszentrum Jülich, Jülich, 2008).

[18] J. K. G. Dhont, G. Gompper, P. Lang, D. Richter, M. Ripoll, D. Willbold, and R. Zorn, eds., *Macromolecular Systems in Soft and Living Matter*, vol. 20 of *Key Technologies* (Forschungszentrum Jülich, Jülich, 2011).

[19] R. Strey, R. Schomäcker, D. Roux, F. Nallet, and U. Olsson, J. Chem. Soc. Faraday Trans. **86**, 2253 (1990).

[20] W. Helfrich, Z. Naturforsch. **33a**, 305 (1978).

[21] C. R. Safinya, D. Roux, G. S. Smith, S. K. Sinha, P. Dimon, N. A. Clark, and A. M. Bellocq, Phys. Rev. Lett. **57**, 2718 (1986).

[22] C. R. Safinya, E. B. Sirota, D. Roux, and G. S. Smith, Phys. Rev. Lett. **62**, 1134 (1989).

[23] G. Gompper and D. M. Kroll, Europhys. Lett. **9**, 59 (1989).

[24] R. Strey, W. Jahn, M. Skouri, G. Porte, J. Marignan, and U. Olsson, in *Structure and Dynamics of Strongly Interacting Colloids and Supramolecular Aggregates in Solution*, edited by S.-H. Chen, J. S. Huang, and P. Tartaglia (Kluwer, Dordrecht, 1992), pp. 351–363.

[25] H. T. Davis, J. F. Bodet, L. E. Scriven, and W. G. Miller, in *Physics of Amphiphilic Layers*, edited by J. Meunier, D. Langevin, and N. Boccara (Springer-Verlag, Berlin, 1987), pp. 310–327.

[26] W. Helfrich, Z. Naturforsch. **28c**, 693 (1973).

[27] L. E. Scriven, Nature **263**, 123 (1976).

[28] P.-G. de Gennes and C. Taupin, J. Phys. Chem. **86**, 2294 (1982).

[29] S. A. Safran, D. Roux, M. E. Cates, and D. Andelman, Phys. Rev. Lett. **57**, 491 (1986).

[30] P. B. Canham, J. Theor. Biol. **26**, 61 (1970).

[31] U. S. Schwarz and G. Gompper, Phys. Rev. E **59**, 5528 (1999).

[32] G. Porte, M. Delsanti, I. Billard, M. Skouri, J. Appell, J. Marignan, and F. Debeauvais, J. Phys. II France **1**, 1101 (1991).

[33] L. Peliti and S. Leibler, Phys. Rev. Lett. **54**, 1690 (1985).

[34] W. Cai, T. C. Lubensky, P. Nelson, and T. Powers, J. Phys. II France **4**, 931 (1994).

[35] F. David, in *Statistical Mechanics of Membranes and Surfaces*, edited by D. R. Nelson, T. Piran, and S. Weinberg (World Scientific, Singapore, 1989), pp. 157–223.

[36] D. C. Morse, Phys. Rev. E **50**, R2423 (1994).

[37] G. Gompper and M. Schick, Phys. Rev. Lett. **65**, 1116 (1990).

[38] M. Teubner and R. Strey, J. Chem. Phys. **87**, 3195 (1987).

[39] M. Teubner, Europhys. Lett. **14**, 403 (1991).

[40] N. F. Berk, Phys. Rev. Lett. **58**, 2718 (1987).

[41] N. F. Berk, Phys. Rev. A **44**, 5069 (1991).

[42] P. Pieruschka and S. A. Safran, Europhys. Lett. **22**, 625 (1993).

[43] R. P. Feynman, *Statistical Mechanics* (Addison-Wesley, Reading, MA, 1972).

[44] J. J. Binney, N. J. Dowrick, A. J. Fisher, and M. E. J. Newman, *The Theory of Critical Phenomena* (Clarendon Press, Oxford, 1992).

[45] P. Pieruschka and S. A. Safran, Europhys. Lett. **31**, 207 (1995).

[46] D. Roux, M. E. Cates, U. Olsson, R. C. Ball, F. Nallet, and A. M. Bellocq, Europhys. Lett. **11**, 229 (1990).

[47] D. Roux, C. Coulon, and M. E. Cates, J. Phys. Chem. **96**, 4174 (1992).

[48] W. Helfrich, J. Phys. France **46**, 1263 (1985).

[49] W. Helfrich, Eur. Phys. J. B **1**, 481 (1998).

[50] Y. Kantor and D. R. Nelson, Phys. Rev. Lett. **58**, 2774 (1987).

[51] Y. Kantor and D. R. Nelson, Phys. Rev. A **36**, 4020 (1987).

[52] J. Lidmar, L. Mirny, and D. R. Nelson, Phys. Rev. E **68**, 051910 (2003).

[53] G. Gompper and D. M. Kroll, J. Phys. I France **6**, 1305 (1996).

[54] G. Gompper and D. M. Kroll, in *Statistical Mechanics of Membranes and Surfaces*, edited by D. R. Nelson, T. Piran, and S. Weinberg (World Scientific, Singapore, 2004), pp. 359–426, 2nd ed.

[55] G. Gompper and D. M. Kroll, Phys. Rev. Lett. **81**, 2284 (1998).

[56] M. Peltomäki, G. Gompper, and D. M. Kroll, preprint (2012).

[57] A. G. Petrov, M. D. Mitov, and A. Derzhanski, Phys. Lett. A **65**, 374 (1978).

[58] G. Porte, J. Appell, P. Bassereau, and J. Marignan, J. Phys. France **50**, 1335 (1989).

[59] R. Strey, Colloid Polym. Sci. **272**, 1005 (1994).

[60] M. Skouri, J. Marignan, J. Appell, and G. Porte, J. Phys. II France **1**, 1121 (1991).

[61] B. Jakobs, T. Sottmann, R. Strey, J. Allgaier, L. Willner, and D. Richter, Langmuir **15**, 6707 (1999).

[62] T. Auth and G. Gompper, Phys. Rev. E **68**, 051801 (2003).

[63] H. Endo, J. Allgaier, G. Gompper, B. Jakobs, M. Monkenbusch, D. Richter, T. Sottmann, and R. Strey, Phys. Rev. Lett. **85**, 102 (2000).

[64] H. Endo, M. Mihailescu, M. Monkenbusch, J. Allgaier, G. Gompper, D. Richter, B. Jakobs, T. Sottmann, R. Strey, and I. Grillo, J. Chem. Phys. **115**, 580 (2001).

[65] G. Gompper, D. Richter, and R. Strey, J. Phys.: Condens. Matter **13**, 9055 (2001).

[66] C. Hiergeist and R. Lipowsky, J. Phys. II France **6**, 1465 (1996).

[67] E. Eisenriegler, A. Hanke, and S. Dietrich, Phys. Rev. E **54**, 1134 (1996).

[68] L. D. Landau and E. M. Lifshitz, *Theory of Elasticity* (Addison-Wesley, Reading, MA, 1959).

[69] S. T. Milner and T. A. Witten, J. Phys. France **49**, 1951 (1988).

[70] G. Gompper, H. Endo, M. Mihailescu, J. Allgaier, M. Monkenbusch, D. Richter, B. Jakobs, T. Sottmann, and R. Strey, Europhys. Lett. **56**, 683 (2001).

[71] M. Klostermann, T. Foster, R. Schweins, P. Lindner, O. Glatter, R. Strey, and T. Sottmann, Phys. Chem. Chem. Phys. **13**, 20289 (2011).

[72] O. Holderer, M. Klostermann, M. Monkenbusch, R. Schweins, P. Lindner, R. Strey, D. Richter, and T. Sottmann, Phys. Chem. Chem. Phys. **13**, 3022 (2011).

[73] M. Kerscher, P. Busch, S. Mattauch, H. Frielinghaus, D. Richter, M. Belushkin, and G. Gompper, Phys. Rev. E **83**, 030401(R) (2011).

[74] M. Belushkin and G. Gompper, J. Chem. Phys. **130**, 134712 (2009).

[75] D. J. Amit, *Field Theory, the Renormalization Group, and Critical Phenomena* (World Scientific, Singapore, 1984).